

Probing the mass-loss history of the unusual Mira variable R Hydrae through its infrared CO wind[★]

L. Decin^{1,2,★★}, L. Blomme¹, M. Reyniers^{1,★★}, N. Ryde^{3,4}, K. H. Hinkle⁵, and A. de Koter²

¹ Department of Physics and Astronomy, Institute of Astronomy, K.U. Leuven, Celestijnenlaan 200D, 3001 Leuven, Belgium
e-mail: Leen.Decin@ster.kuleuven.ac.be

² Sterrenkundig Instituut Anton Pannekoek, University of Amsterdam, Kruislaan 4031098 Amsterdam, The Netherlands

³ Department of Astronomy and Space Physics, Uppsala University, Box 515, 5120 Uppsala, Sweden

⁴ Lund Observatory, Box 43, 22100 Lund, Sweden

⁵ National Optical Observatories, PO Box 26732, Tucson, ZA 85726, USA

Received 21 December 2007 / Accepted 23 March 2008

ABSTRACT

Context. The unusual Mira variable R Hya is well known for its declining period between AD 1770 and 1950, which is possibly attributed to a recent thermal pulse.

Aims. The goal of this study is to probe the circumstellar envelope (CSE) around R Hya and to check for a correlation between the derived density structure and the declining period.

Methods. We investigate the CSE around R Hya by performing an in-depth analysis of (1.) the photospheric light scattered by three vibration-rotation transitions in the fundamental band of CO at 4.6 μm ; and (2.) the pure rotational CO $J = 1-0$ through 6-5 emission lines excited in the CSE. The vibrational-rotational lines trace the inner CSE within 3.5'', whereas the pure rotational CO lines are sensitive probes of the cooler gas further out in the CSE.

Results. The combined analysis bears evidence of a change in mass-loss rate some 220 yr ago (at $\sim 150 R_\star$ or ~ 1.9 arcsec from the star). While the mass-loss rate before AD 1770 is estimated to be $\sim 2 \times 10^{-7} M_\odot/\text{yr}$, the present day mass-loss rate is a factor of ~ 20 lower. The derived mass-loss history nicely agrees with the mass-loss rate estimates by Zijlstra et al. (2002) on the basis of the period decline. Moreover, the recent detection of an AGB-ISM bow shock around R Hya at 100 arcsec to the west by Wareing et al. (2006) shows that the detached shell seen in the 60 μm IRAS images can be explained by a slowing-down of the stellar wind by surrounding matter and that no extra mass-loss modulation around 1–2 arcmin needs to be invoked.

Conclusions. Our results give empirical evidence to the thermal-pulse model, which is capable of explaining both the period evolution and the mass-loss history of R Hya.

Key words. line: profiles – radiative transfer – stars: AGB and post-AGB – stars: circumstellar matter – stars: mass-loss – stars: individual: R Hya

1. Introduction

The variability of R Hya (HR 5080, IRAS 13269-2301, HIP 65835) was first established in the early 1700s by Cassini's nephew Miraldi (Zijlstra et al. 2002) and was later classified as a Mira variable. Mira variables show a mono-periodic light curve with large visual amplitudes of more than 2.5 mag, and are usually found near the tip of the asymptotic giant branch (AGB). The s-process element technetium (^{99}Tc) was detected in R Hya by Little et al. (1987) indicating that the star is in the *thermal pulsing* phase of the AGB. It is well established that AGB stars lose a significant amount of mass during the AGB phase due to a dust driven wind (e.g., Habing 1996).

The star R Hya belongs to the group of optically visible 1n M stars in the IRAS-LRS catalog (Olson et al. 1986). The (almost) absence of the silicate feature around 10 μm (see Fig. 2) and its IRAS colours suggest that the dusty circumstellar envelope is *detached* from the central star (Hashimoto et al. 1990). From modelling the spectral energy distribution (SED), Hashimoto et al. (1990) derived an inner radius of $60 R_\star$

(i.e. $\sim 1.8''$), based on a distance of 110 pc and a stellar radius R_\star of $700 R_\odot$. Moreover, R Hya is an unusual Mira variable, being well known for its *declining period* between AD 1770 and 1950 (Zijlstra et al. 2002), possibly attributed to a recent *thermal pulse* (Wood & Zarro 1981). The gradual change in the period of R Hya implies that its pulsation mode has remained constant over the last 345 years. The period evolution should therefore be related to a change in stellar parameters, causing a *variation* in the mass-loss rate during the last few hundred years (using, e.g., the mass-loss equations as derived by Vassiliadis & Wood 1993; Blöcker 1995).

Apart from mass-loss rate variations being caused by an *internal* mechanism (e.g., a thermal pulse or non-linearity effects due to the pulsations), the interaction of the AGB wind with the interstellar medium (ISM) forms another explanation for large detached shells (Young et al. 1993). Recently, Wareing et al. (2006) detected a bow shock around R Hya: Spitzer images revealed a one-sided parabolic arc 100'' to the west, stretching from north to south.

Thanks to the large cosmic abundances of carbon and oxygen and the high dissociation energy of carbon monoxide (CO), the CO molecule is ubiquitous in the CSE around evolved stars, being present both in the cool outer layers and in the warmer inner

[★] Appendix A is only available in electronic form at <http://www.aanda.org>

^{★★} Postdoctoral Fellow of the Fund for Scientific Research, Flanders.

regions where the wind is initiated. CO studies have therefore been extensively used to trace the structure in the CSEs around evolved stars. Since the late seventies, low-excitation *rotational* CO emission lines were used to estimate the mass-loss rates during the AGB phase (e.g. Zuckermann et al. 1977; Morris 1980; Knapp et al. 1980).

The circumstellar shells can also be imaged in photospheric light scattered by atomic or molecular resonance lines, including CO (e.g., Plez & Lambert 1994; Gustafsson et al. 1997). Ryde et al. (2000) have recently applied this latter technique to study the intermediate regions of the CSE of *o* Ceti (Mira) using three *vibration-rotation* transitions of the fundamental band of $^{12}\text{C}^{16}\text{O}$ between low-lying rotational levels in the ground and first vibrationally excited state¹. The infrared vibration-rotation lines of CO, as an alternative to pure rotational CO lines at millimeter wavelengths, allow us to study the regions closer to the star and they admit higher spatial resolution in single-telescope studies. Vibration-rotation lines are excited close to the star and are sensitive to the radiation field, whereas pure rotational lines are usually more sensitive to the temperature structure further out in the envelope. By combining observations of pure rotational and vibration-rotation CO lines, one may sample the gas located at $\sim 1''$ distance from the star and beyond, and one might be able to put constraints on the temperature and density stratification in the whole envelope, and hence on possible mass-loss rate variations in the CSE of the studied object.

We seek to derive the mass-loss history of R Hya from the observations and in-depth modelling of pure rotational and vibrational-rotational CO lines emitted in the envelope around R Hya. In Sect. 2, we first discuss the scattered low-excitation vibrational-rotational transitions of the fundamental band of CO observed in the CSE around R Hya with the Phoenix spectrograph. Thereafter, in Sect. 2.2, we look at the pure rotational CO transitions emitted further out in the envelope of R Hya. In Sect. 3, both the vibrational-rotational and pure rotational CO lines are modelled using a non-LTE radiative transfer code. The results are discussed in Sect. 4 and some conclusions are drawn in Sect. 5.

2. Observational data

The analysis is based on two sets of observations probing different regions of the CSE. First, the CSE is imaged in photospheric light scattered by low-excitation vibrational-rotational transitions of the fundamental band of CO at an angular distance, β , between $\sim 1''$ – $3.5''$ (see Sect. 2.1). Second, radio data of pure rotational CO emission lines are analysed in detail (see Sect. 2.2). The latter data provide constraints on the outer regions of the CSE, out to approximately $2500R_*$ away from the star. Moreover, the circumstellar structure of R Hya has been investigated in the IRAS survey scan data and the spectral energy distribution (SED) has been modelled by Hashimoto et al. (1998). Since the dust emission has already been analysed by Hashimoto et al. (1998) and the model fit was repeated and confirmed by Zijlstra et al. (2002), we only summarise the most important dust characteristics and the main results of the dust analysis done by these two research groups in Sect. 2.3.

¹ Since this paper only deals with $^{12}\text{C}^{16}\text{O}$ and no other isotopes, the isotopic notation will be omitted.

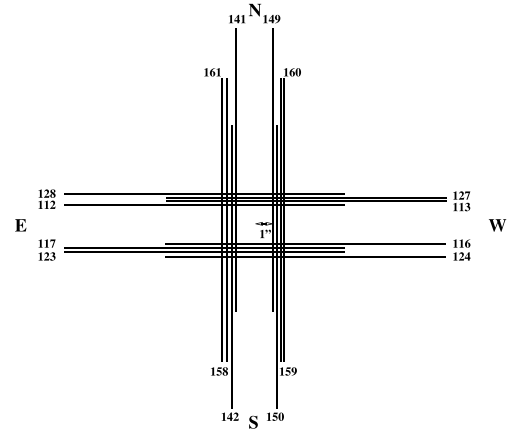


Fig. 1. Slit positions for the Phoenix off-star observations of R Hya. All off-star slits are positioned at $1''$ from the star. In the figure, the slits are shifted for reasons of clarity. The number of each data set as used in the logbook (Table A.1) is indicated.

2.1. CO vibrational-rotational transitions

We observed on 26 February 2005 with the Phoenix² spectrometer mounted on the 8 m Gemini South telescope. Phoenix is a single-order, high spectral resolution ($R \sim 50\,000$ – $75\,000$), near-IR (1 – $5\,\mu\text{m}$) spectrometer (Hinkle et al. 1998). The slit length is $14''$. For our observations, a slit width of 2 pixels ($0.17''$) is used, resulting in a resolution of $\sim 75\,000$. The visual seeing was around $0.6''$. Assuming that the seeing is proportional to the wavelength to the $1/5$ power (Roddiier 1981), the seeing was better than $0.4''$ at $4.6\,\mu\text{m}$, the wavelength of the observation.

Low-excitation lines of the vibration-rotation fundamental R-branch of the electronic ground state of CO are observed. The selected lines are the 1–0 R(1) (i.e., $v = 1 \rightarrow 0$ and $J' = 2 \rightarrow J'' = 1$) at $2150.86\,\text{cm}^{-1}$; the 1–0 R(2) at $2154.60\,\text{cm}^{-1}$; and the 1–0 R(3) at $2158.30\,\text{cm}^{-1}$.

We used the same observational set-up as in Ryde et al. (2000). The CSE of R Hya is observed in a hashed configuration, resembling a perpendicular railway crossing with the star in the middle (see Fig. 1). The long slit was placed in the off-star position at $1''$ from the star. The four slit positions overlap at a distance of $\sim 1.4''$ from the star. We were able to detect emission in the CSE out to $\sim 3.5''$.

The observed CO R(1), R(2), and R(3) lines suffer from telluric absorption. Therefore, at the time of observation, the radial velocity of the star combined with the heliocentric velocity of the Earth must shift the star's CO lines away from the telluric ones. Otherwise, the blending of the telluric and stellar lines severely compromises the analysis of the faint circumstellar emission. From the pure rotational CO lines, we deduce a $v_{\text{LSR}} = -10.4\,\text{km s}^{-1}$ (see Sect. 2.2). At the time of the observations and at Gemini South, this corresponds to a geocentric radial velocity of $-33.5\,\text{km s}^{-1}$.

The exposure times for the on-star observations were 1 s and were 30 s for each of the off-star observations. The total amount of observing time was ~ 5 h, of which some 650 s were effective observing time on the target. We used the on-star exposures to remove the scattered light from the off-star exposures. Since Phoenix is a long-slit spectrograph, nodding along the slit is

² Based on observations with Phoenix, NAOJ's high-resolution infrared spectrograph mounted on Gemini South. Program ID is GS-2005A-C-8, observing time: 20 h.

possible. This mode has been used to subtract the background (see also Sect. 2.1.1). A logbook of the observations can be found in Table A.1 in the online Appendix A. We used the following nomenclature to describe the off-star observations: “EW-slit N1 E2.5” indicates a slit-position oriented in the east-west direction, which is offset by 1” to the north from the star and which has been moved 2.5” in the east-direction along the slit (data sets 112 and 128 in Fig. 1). As can be seen in the logbook, we have 16 off-star observations at our disposal: each time four observations with a slit positioned 1” to the north, south, east, and west away from the star were taken. The observing numbers of the off-star data sets are listed in the logbook, and schematically represented in Fig. 1.

2.1.1. Data reduction

The data reduction is based on the standard procedures provided by the Image Reduction and Analysis Facility (IRAF). For a full description of the reduction procedure we refer to Ryde et al. (2000); only the most important steps and differences we outline here. Since the absolute flux calibration contains several steps, this part of the reduction process is outlined in a separate section. The pointing accuracy is discussed in Sect. 2.1.3.

Sky subtraction. To remove the thermal sky spectrum from the on- and off-star data, two methods can be applied. Either, (i.) one takes an exposure of the sky, for our observations taken at 15” from the star; or (ii.) one chooses to nod along the slit. Due to the variable seeing at the moment of the observations this second option usually gives the most accurate results with two consecutive exposure frames. We only used the first option when the starlight was received in the middle of the slit (data sets 158, 159, 160, 161, see Fig. 1).

Wavelength calibration. The wavelength calibration is based on the observations of the telluric reference star, β Ori, a B8Iab star. The spectrum of a hot telluric star is essentially a continuum around $4.6\mu\text{m}$, which can be well-fitted by a blackbody. The only spectral features in the spectrum are due to telluric absorption lines. Telluric CO and H₂O lines in the β Ori spectrum are identified and the pixels are converted to (the vacuum laboratory) wavelengths. The uncertainty in the wavelength scale is $\sim 0.07\text{ cm}^{-1}$ or 9.5 km s^{-1} .

2.1.2. Absolute flux calibration

Different steps are involved in the absolute flux calibration process of the on-star and off-star data. After the conversion factors are determined to convert the on-star data to physical flux units, the off-star data are scaled with the same factor.

Slit loss. To determine the amount of light caught in a 2-pixel spectrograph slit, a comparison is made between the on-star data of the B-type star α Vir observed with either a 2-pixel slit or without slit. The flux received in a 2-pixel slit is derived to be 38% of the flux when no slit is used, hence yielding a slit loss of 62%.

Flux calibration of the on-star spectra. The low-resolution Infrared Space Observatory – Short Wavelength Spectrometer

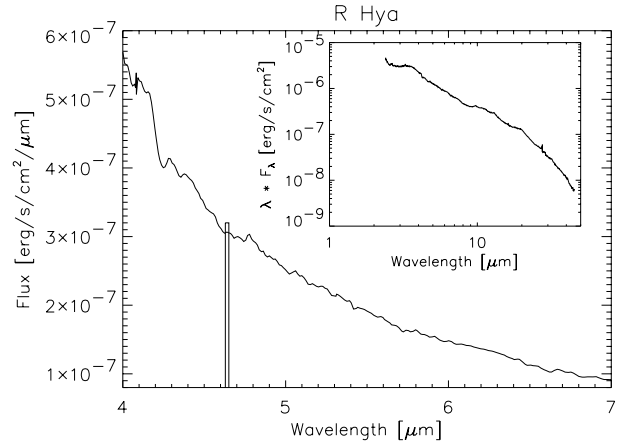


Fig. 2. The low-resolution ISO-SWS spectrum ($R \sim 100$) in the 4 to $7\mu\text{m}$ wavelength range. The width of the box denotes the observed spectral range of the Phoenix spectrometer. The inset shows the full ISO-SWS spectrum between 2.38 and $45.2\mu\text{m}$ in the $(\lambda \times F_\lambda)$ -space illustrating the absence of the $10\mu\text{m}$ silicate feature.

(ISO-SWS)³ data of R Hya are used to flux-calibrate the on-star spectra. R Hya has been observed on February, 7 1996 by the ISO-SWS (TDT 8200502), see Fig. 2. After normalising the on-star data and taking into account the 62% slit loss, a flux conversion factor of $1.2 \times 10^{-7}\text{ erg s}^{-1}\text{ cm}^{-2}\mu\text{m}^{-1}$ per detector count is derived. The total flux calibration is then given by the normalising spline and this flux conversion factor.

Comparison with the MARCS model spectrum. To further check the absolute flux calibration, a comparison is made with a MARCS spherical model atmosphere (Gustafsson et al. 1975, and further updates). Stellar parameters for R Hya as derived and discussed by Zijlstra et al. (2002) have been used: an effective temperature $T_{\text{eff}} = 2830\text{ K}$; a radius $R = 450R_\odot$; a luminosity $L = 1.16 \times 10^4 L_\odot$; a gravity $\log g = -0.56$; a mass $M = 2M_\odot$; and a distance $D = 165\text{ pc}$. For the spectrum synthesis, the same atomic and molecular databases as in Decin & Eriksson (2007) were used, the only difference being the H₂O line list. For this analysis, the SCAN H₂O line list of Jørgensen et al. (2001) was used (instead of the AMES H₂O line list of Partridge & Schwenke 1997). As noted by Jørgensen et al. (2001) and Aringer et al. (2002), the SCAN H₂O linelist better reproduces the slopes observed in the infrared spectra of M-giants (see also the inset of Fig. 3), although the predicted energy levels of the AMES line list are more accurate (e.g., Jones et al. 2003). We also note that for the purpose of this work the CO line list computed by Goorvitch & Chackerian (1994) is used.

In Fig. 3, a comparison is shown between several theoretical spectra to illustrate the effect of the effective temperature on the infrared spectrum. We find that a theoretical spectrum with $T_{\text{eff}} = 2800\text{ K}$ already nicely reproduces the ISO-SWS spectrum. Note that it is not our purpose to perfectly match the ISO-SWS spectrum, especially since the hydrostatic MARCS model atmosphere code does not account for the effects of pulsations in the Mira-type star R Hya.

In Fig. 4, the same theoretical spectrum as in Fig. 3 (with $T_{\text{eff}} = 2800\text{ K}$) is compared with the observed on-star Phoenix

³ Based on observations with ISO, an ESA project with instruments funded by ESA Member States (especially the PI countries: France, Germany, The Netherlands and the United Kingdom) and with the participation of ISAS and NASA.

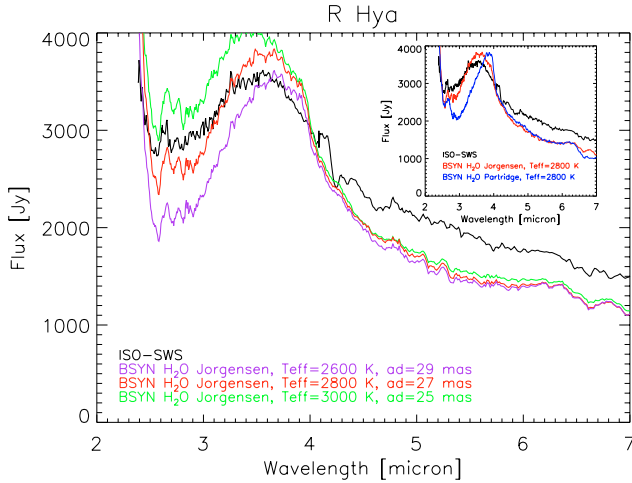


Fig. 3. Comparison between the ISO-SWS spectrum of R Hya and theoretical model spectra computed with the MARCS code. The black curve represents the ISO-SWS spectrum, the purple curve a MARCS spectrum at $T_{\text{eff}} = 2600$ K and angular diameter $ad = 29$ mas, the red curve at $T_{\text{eff}} = 2800$ K and $ad = 27$ mas, and the green curve at $T_{\text{eff}} = 3000$ K and $ad = 25$ mas. The inset shows a comparison between the ISO-SWS spectrum of R Hya (black), the theoretical spectrum with $T_{\text{eff}} = 2800$ K and the SCAN H₂O linelist of Jørgensen et al. (2001) (red) and the theoretical spectrum with $T_{\text{eff}} = 2800$ K and the H₂O linelist of Partridge & Schwenke (1997) (blue).

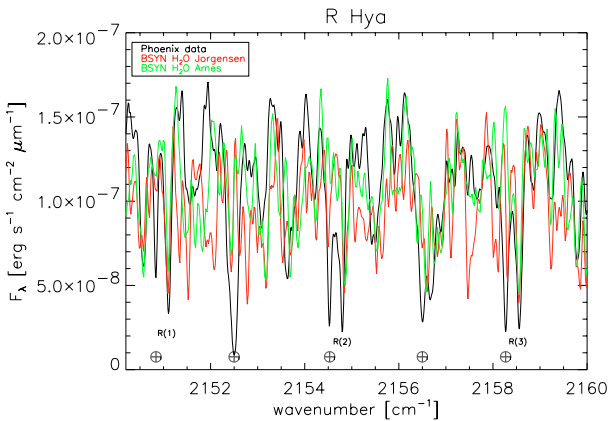


Fig. 4. Comparison between the on-star Phoenix spectrum of R Hya and the theoretical MARCS model spectrum computed with the SCAN H₂O linelist (red) and the AMES H₂O linelist (green) at a T_{eff} of 2800 K and an angular diameter of 27 mas. The three photospheric CO R(1), R(2), and R(3) lines are indicated. Telluric H₂O and CO lines are marked with a “ ϕ ” symbol. The stellar CO lines are shifted out of the telluric ones, with a geocentric radial velocity of -32.3 km s⁻¹.

spectrum of R Hya. The general features are well reproduced and are mainly due to photospheric water and CO. Moreover, the agreement of the overall flux level is astonishingly good: while Ryde et al. (2000) have multiplied the model fluxes with a factor of 1.4 to adapt the theoretical MARCS spectrum to the observed spectrum of *o* Ceti, no (extra) shift needs to be applied to match the observed Phoenix and theoretical MARCS spectrum of R Hya. Comparing the shift between the telluric and photospheric CO lines in Fig. 4 yields a radial velocity of -32.3 km s⁻¹, in excellent agreement with the value derived in Sect. 2.1.

Flux calibration of the off-star data. The off-star data are flux-calibrated using the flux calibration as deduced for the on-star data, but taking into account the exposure time of 30 s for the off-star data (compared to the 1 s exposure time of the on-star data).

Uncertainties in the absolute flux calibration and CO emission lines. Each of the steps involved in the flux calibration is subject to uncertainties, in particular since R Hya is a pulsating Mira-type star. The absolute uncertainty for each off-star and on-star spectrum is estimated to be $\sim 20\%$ when no pointing errors are taken into account. The CO emission lines, being the result from subtracting the scaled on-star spectrum from an off-star spectrum (see Sect. 2.1.4) are estimated to be uncertain within 10%, and somewhat larger at the edges of the detector due to the higher uncertainty in the flat-fielding. An uncertainty in the slit position of $0.1''$ ($0.2''$, see Sect. 2.1.3), however, yields a 35% (90%) error in the integrated intensity values (assuming an intensity dependence on the angular distance of β^{-3} , see Sect. 3.1). However, the decline of the integrated intensity as a function of the angular distance (see Sect. 2.1.4) will not be affected by this pointing error.

2.1.3. Pointing accuracy

The Gemini telescope guides using a wavefront sensor star that is typically located about 5 arcmin from the target star. The wavefront sensor star is held to $0.01''$ drift in 1 h. This star controls the offsets. So there is essentially no error introduced by the offsetting.

To center a star on the slit, we first imaged the slit against the sky with Phoenix in imaging mode (the grating is by-passed). Then the star is imaged and centered at the middle of the slit position. One then switches from imaging mode to spectroscopy mode, moves the star to the correct starting position on the slit and starts taking spectra. The plate scale has very small pixels allowing us to position the star to better than $0.1''$ on the slit. This peak-up happened before the on-star exposure 108, before data set 123, before the on-star exposure 137, before data set 149, and before data set 158.

The wavefront sensor (WFS) of Phoenix is not inside Phoenix, but in the telescope. This implies that there can be flexure between the Phoenix spectrometer and the telescope. From about 7 to 9 h UTC, we observed at a changing parallactic angle. As a result, observations in this time interval likely suffer from large flexure differences. They are on the order of 0.2 arcsec over an hour, but they may occur suddenly. To check this, after we had finished the sequence of observations 141 through 152, we repeated the offsets in an abbreviated way with data sets 158 through 161. As will be discussed in Sect. 2.1.5, flexure problems likely have occurred in data sets (149, 150).

2.1.4. Observational results

To study the CO emission lines excited in the CSE, the on-star data are scaled to the off-star data and subtracted. This is illustrated in Fig. 5 for the EW-slit S1 W2.5 (data set 124). The scaled on-star spectrum at least approximately represents the radiation exciting the molecules. The CO and H₂O lines dominate the photospheric spectrum (Aringer et al. 2002). The off-star spectrum consists of (1.) stellar light that is scattered in the Earth’s atmosphere, the telescope, the spectrometer and/or dust grains in the CSE, leading to a spectrum resembling the

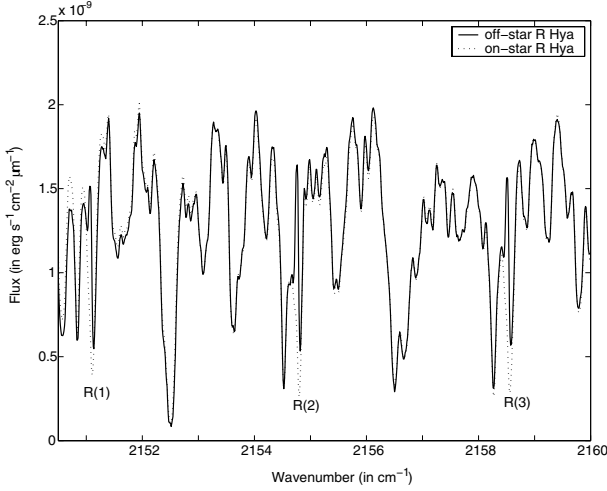


Fig. 5. Off-star (full line) and on-star (dashed line) spectrum of R Hya. The three off-star CO vibration-rotation emission lines, which are marked R(1), R(2), and R(3), are partly filled in by emission from the circumstellar CO lines compared to the on-star observations. Telluric CO lines are at 2150.86, 2154.60 and 2158.30 cm^{-1} , telluric H_2O lines at 2152.50 and 2156.50 cm^{-1} .

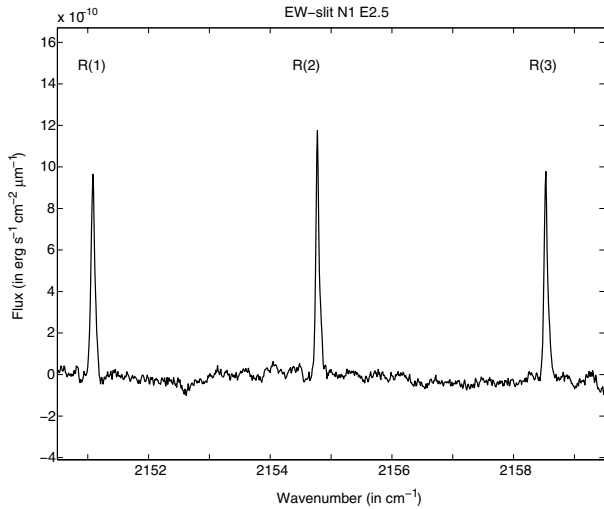


Fig. 6. The resulting circumstellar CO vibration-rotation flux from the wind of R Hya for data set 128, being a EW-slit N1 E2.5. The intensity is integrated over the full slit area.

on-star one; and (2.) the CO 1–0 R(1), R(2), and R(3) vibration-rotation emission lines. The circumstellar molecules are hence radiatively excited by the stellar light.

Figure 6 shows a typical example of the resulting CO emission lines integrated over the long slit for data set 128, being a EW-slit N1 E2.5. The CO emission lines from the other 15 data sets are displayed in Figs. A.1–A.4 in the online appendix. Note that the (co-)ordinate axes are put in the same scale in these plots to strengthen the (dis)similarities between the different off-star observations. Variations in the telluric lines between the object frame exposure and the background exposure, between two successive exposures used for background subtraction, and/or between the on-star and off-star exposure result in non-zero residuals in the continuum between the CO lines. The signal-to-noise ranges between 5 and 30.

In order to study the CO emission as a function of the angular distance β from the star, we divided the long-slit spectra into 38 sub-spectra. Each sub-spectrum covers 2 pixels in the

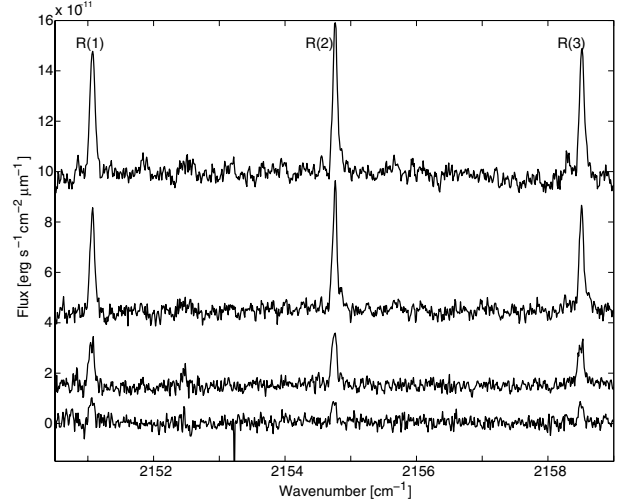


Fig. 7. Set of emission spectra at the east-position from R Hya (data set 142, being a NS-slit E1 S2.5). The spectra are shifted vertically for reasons of clarity. The top spectrum is measured closest to the star, i.e., at $\beta = 1''$. The subsequent spectra are measured at 1.1'', 1.6'' and 2.4'' from the star.

spatial direction. Thisway, the emission between 1'' and 3.5'' from the star can be measured (see, e.g., Fig. 7). For each of the 38 sub-spectra, the wavelength-integrated intensity of the lines is measured, taken into account the $2^{\#}2$ pixel area. This way, each of the 16 off-star data sets gives us the decline of the intensity of the three CO emission lines as a function of the angular distance, β , in two directions, e.g., data set 112 taken at the north of R Hya yields the decline in the north-east (NE) and north-west (NW) direction⁴. The three CO emission lines, R(1), R(2), and R(3) yield analogous results. By adding the intensities of the three lines, the signal-to-noise is increased. The decline of the intensity in the four slits positioned at 1'' to the north of R Hya is displayed in Fig. 8. The results for the other three directions are displayed in the Figs. A.5–A.7 in the online appendix. An overview of the mean of the eight different directions, together with the overall mean and standard deviation, is displayed in Fig. 9.

2.1.5. Discussion

In this section, we first will discuss the decline of the intensity in the different scan directions and compare the different data sets tracing the same geometrical region in the circumstellar envelope. Thereafter, the mean over all directions will be compared to the mean of each individual direction. The data will be modelled and analysed in detail in Sect. 3.

Inspecting Fig. 8 and the online Fig. A.5 displaying the circumstellar CO vibration-rotation emission integrated over the slit positioned at, respectively, 1'' north and south away from the star, it is clear that the four data sets tracing the same region in the CSE match nicely. The scatter between the data sets is mainly due to small inaccuracies in the slit position and the (slightly) variable sky conditions. The north-west (south-east) direction have a higher intensity further out in the CSE than the north-east (south-west) direction.

⁴ The nomenclature for the position of the slit used throughout the remainder of the paper is as follows: e.g., (NE) denotes a slit-position which is offset by 1'' to the north, and for which we are scanning to eastern part of the slit. Hence, the first symbol denotes the offset direction, the second symbol denotes the scanning direction.

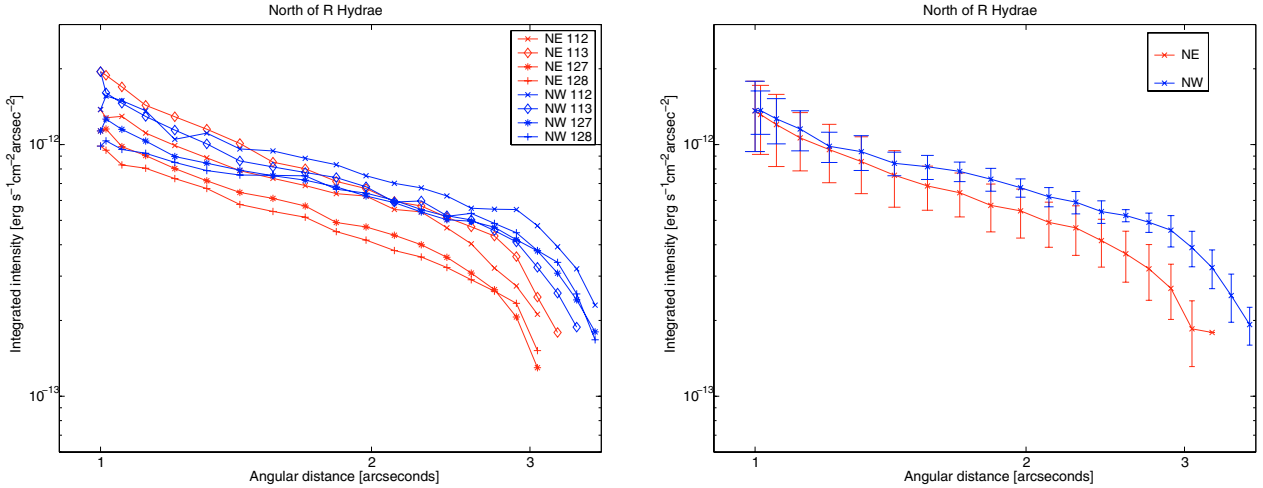


Fig. 8. Decline of the intensity of the circumstellar emission as a function of angular distance β in the four slits positioned $1''$ to the north of R Hya. *Left:* the decline of the intensity of the four data sets 112 (EW-slit N1 E2.5), 113 (EW-slit N1 W2.5), 127 (EW-slit N1 W2.5), and 128 (EW-slit N1 E2.5) is displayed. *Right:* mean (and standard deviation) of the intensity decline of the four north-east (NE) and north-west (NW) scans.

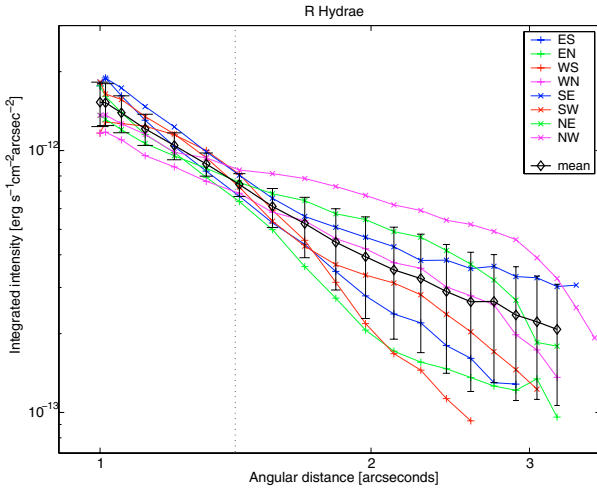


Fig. 9. Decline of the intensity of the circumstellar emission as a function of the angular distance β for the star for eight scan directions. The statistical error bars have been omitted for reasons of clarity. Note that data set 149 (NS-slit W1 N2.5) and 15 (NS-slit W1 S2.5) are omitted (see text for more details). The black line represents the mean (and standard deviation) of the eight scan directions.

Figure A.6, tracing the scans in the east direction of the star, clearly shows a discrepancy between the (141, 142) and (158, 161) data sets in the east-south direction. This shift in intensity is not seen in the east-north direction. The difference between both pairs of data sets can also be seen in the online Fig. A.3, where the (158, 161) data sets show a higher flux peak in all three CO emission lines than the (141, 142) data sets. Flexure between the telescope and the Phoenix slit (see Sect. 2.1.3) is probably the cause for this discrepancy. Note also that the nodding principle was used to subtract the sky from the (141, 142) data set, while for the (158, 161) data set the sky was subtracted using a sky frame exposure taken at $15''$ from the star.

A similar problem as for the east direction is seen in Fig. A.7 tracing the westward region in the CSE. A good match is found for the four data sets tracing the west-north direction, but the west-south scans largely differ. While for the east-south scans in Fig. A.6 only a shift in the absolute integrated intensity value

between the different data sets is noted, the intensity decline of the (159, 160) data sets is much steeper than for the (149, 150) data sets. Inspecting the cross-over points between the west-south and south-west direction around $1.4''$ from the star clearly points towards problems with the (149, 150) data sets (see Fig. A.8), possibly caused by a sudden change in flexure between the telescope and the Phoenix slit. Moreover, while all the other scan directions show the same trend in intensity decline (see also next paragraph), the (149, 150) data sets are atypical. In the further analysis, the (149, 150) data sets have, therefore, been omitted. By comparing the cross-overs of the other scan directions, a maximum uncertainty in slit-position of $0.2''$ is derived.

In Fig. 9, the mean of the intensity decline over all directions is compared to the mean over all individual directions. Inspecting Fig. 9, we conclude that the measured emission-line intensities in the different directions from the star are consistent with a *symmetric* wind. The fact that the NW, NE, and SE intensities lie above the mean, while the SW, ES, EN, and WS lie below may be a (tentative) suggestion for a bipolar structure stretching from NW to SE.

2.2. CO rotational transitions

CO pure rotational line profiles ($J = 2-1$ and $3-2$) have been observed with the 15 m JCMT⁵. The observations were carried out using a position-switching mode. The JCMT data reduction was performed with the SPLAT devoted routines of STARLINK. A polynomial of first order was fitted to an emission-free region of the spectral baseline and subtracted. The antenna temperature, T_A^* , was converted to the main-beam temperature ($T_{mb} = T_A^*/\eta_{mb}$), using a main-beam efficiency η_{mb} of 0.69 for the CO ($2-1$) line and of 0.63 for the CO ($3-2$) line. The half-power beamwidth (*HPBW*) of the different receivers was $19.7''$ for CO ($2-1$) and $13.2''$ for CO ($3-2$) (Kemper et al. 2003). The absolute flux calibration accuracy was estimated to be 10%. We note that, in principle, pointing uncertainties, beam effects,

⁵ The James Clerk Maxwell Telescope (JCMT) is operated by The Joint Astronomy Centre on behalf of the Science and Technology Facilities Council of the UK, the Netherlands Organisation for Scientific Research, and the National Research Council of Canada. Program ID is m04an20.

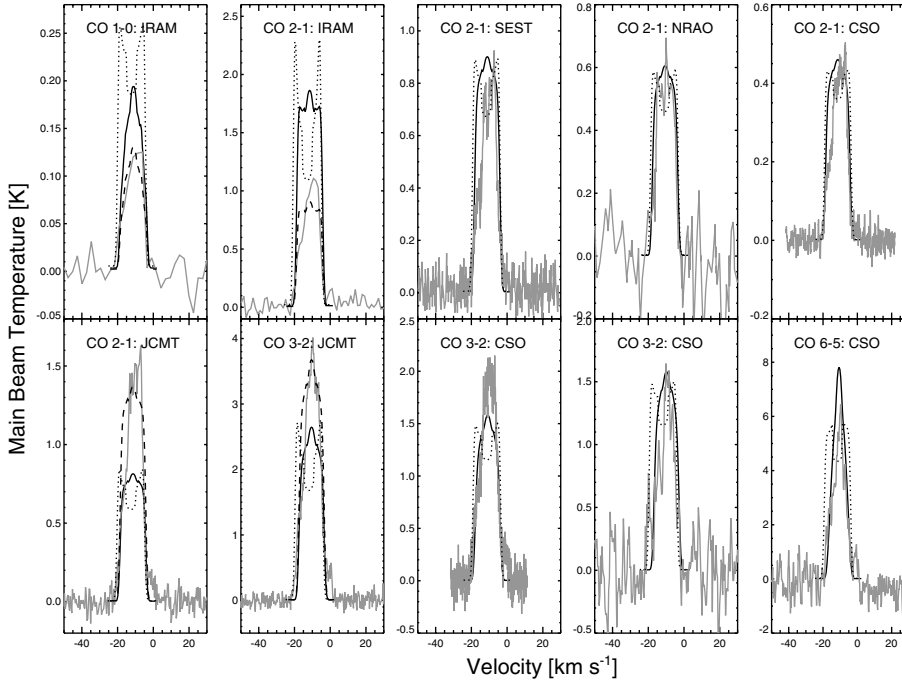


Fig. 10. CO rotational line profiles of R Hya (plotted in grey, see Table 1) compared with (i) black dotted line: the model predictions based on the parameters as given by Wannier & Sahai (1986), who derived a constant mass loss of $\dot{M} \sim 1 \times 10^{-7} M_{\odot} \text{ yr}^{-1}$ using a distance of 130 pc; (ii) full black line: the best-fit model with parameters as specified in Table 3; and (iii) black dashed line: the best-fit model scaled to the observations to illustrate the similarity in line profiles. This scaling is performed only for the IRAM and JCMT data (see text for more details). The rest frame of the velocity scale is the local standard of rest (LSR) velocity.

Table 1. CO rotational line profiles as used in this study. Consecutive columns list the transition, the telescope, the half-power beamwidth (HPBW), the main-beam efficiency (η_{MB}), the absolute flux uncertainty (σ_{abs}), and the literature reference. The beam width, main-beam efficiency, and absolute flux uncertainty listed in this table are the ones as found in the cited paper. In case the absolute flux uncertainty was not given, an uncertainty of 20% is assumed.

Transition	Telescope	HPBW	η_{MB}	σ_{abs}	Literature reference
CO(1–0)	IRAM	23''	0.79	20% ^a	D. Teyssier (<i>priv. comm.</i>)
CO(2–1)	JCMT	19.7''	0.69	20%	this paper
CO(2–1)	IRAM	13''	0.60	20% ^a	D. Teyssier (<i>priv. comm.</i>)
CO(2–1)	SEST	23''	0.50	20% ^a	Winters et al. (2003)
CO(2–1)	NRAO	25''	0.33 ^b	30%	Wannier & Sahai (1986)
CO(2–1)	CSO	30''	0.76	20% ^a	Knapp et al. (1998)
CO(3–2)	JCMT	13.2''	0.63	20%	this paper
CO(3–2)	CSO	20''	0.65	20% ^a	Knapp et al. (1998)
CO(3–2)	CSO	21''	0.65	20%	Teyssier et al. (2006)
CO(6–5)	CSO	12''	0.55	30%	Teyssier et al. (2006)

^a Assumed, ^b taken from Huggins & Healy (1986).

atmospheric seeing, and systematics at these frequencies can combine to produce an error that is larger than 10%. For that reason, a conservative absolute error estimate of 20% is adapted. The line shapes and widths are, however, not very sensitive to pointing errors, etc.

We complemented these data with CO pure rotational line profiles as available in the literature (see Table 1). The object R Hya was observed by different authors, resulting in a total of 10 line profiles covering 4 different transitions. Comparing the different line profiles of one rotational transition gives us information on the absolute flux uncertainties.

All available pure rotational CO emission data of the CSE around R Hya are displayed in Fig. 10 and are compared with a constant mass-loss model (see Sect. 3.2.1) based on the parameters as given by Wannier & Sahai (1986). They derived a constant mass-loss rate of $\dot{M} \sim 1 \times 10^{-7} M_{\odot} \text{ yr}^{-1}$, using a distance of 130 pc based on CO(2–1) data obtained with the NRAO.

While this constant mass-loss rate model is capable of predicting the *integrated intensities* of many of the pure rotational CO lines, it clearly is not able to predict the *line shapes* correctly: the predictions show a “two-horn” line profile (indicative of an optically thin, resolved emission line, Morris 1975) in contrast to the sharp line profiles in the observational data. Comparing, however, the different absolute intensity levels of one rotational transition reveals clear differences (even after correcting for different beam sizes and telescope diameters): the integrated intensities of the CO(2–1) as obtained with the SEST, NRAO, and CSO are well-predicted by the constant mass-loss model, while the same CO(2–1) line observed with IRAM is over-predicted and the one observed with the JCMT is by far under-predicted (see Fig. 10). An analogous problem has been noted by Schöier et al. (2006) for SiO(3–2) observations obtained with IRAM by Bujarrabal et al. (1994), where the IRAM-data were consistently a factor of two lower compared to model predictions matching the other SiO-data. The observations are indeed taken at different phases during the pulsation cycle. However, while the V-band magnitude of R Hya varies between ~ 4 and 10, the amplitude of the variability is typically less in the near-infrared than in the optical, and less in the mid-infrared than in the near-infrared (Smith et al. 2002), and is not expected to have that large an influence on the (sub)millimeter CO lines. When modelling the data, we therefore will give a greater weight to the line shape than to the integrated line intensity, and use the statistical method as developed in Decin et al. (2007) to select the best-fit model (see Sect. 3.2).

2.3. The dust envelope

R Hya is classified as an optically visible $1n$ M star in the IRAS-LRS catalog (Olson et al. 1986), showing (almost) no silicate band feature around $10 \mu\text{m}$ (see Fig. 2). A large number of M-type stars classified as $1n$ have IRAS colours indicating no or optically thin circumstellar dust envelopes with weak mass-loss activity, which explains the (almost) absence of the $10 \mu\text{m}$ silicate feature. Hashimoto et al. (1990), however, found that a

significant fraction of the optically visible $1n$ M stars show remarkably red IRAS photometric colours, which indicate the presence of circumstellar dust. Silicate emission forms close to the star and the lack of it indicates a dust envelope being detached from the central star (Hashimoto et al. 1990). The object R Hya is the brightest source among the red $1n$ M stars. The IRAS images show that the extended emission component around R Hya is almost circular. From modelling the SED, Hashimoto et al. (1990) derived an inner radius of $60 R_\star$ based on a distance of 110 pc and $R_\star = 700 R_\odot$ (i.e. at $\sim 1.8''$). Zijlstra et al. (2002) repeated the SED model fit: at a distance of 165 pc, the inner radius scales to 6×10^{15} cm, and the (pre-AD 1770) mass-loss rate, \dot{M} , is estimated to be $3 \times 10^{-7} M_\odot/\text{yr}$ (assuming a gas-to-dust ratio of 200), with the present-day mass-loss being at least a factor 10 smaller.

Interestingly, the IRAS $60 \mu\text{m}$ image shows a detached shell around a bright point source, with an inner radius of $1\text{--}2$ arcmin (or $1.5\text{--}3 \times 10^{17}$ cm at 165 pc). Hashimoto et al. (1990) cautioned for a possible artefact in the deconvolution procedure, while Zijlstra et al. (2002) considered the case that this ring represents a much older mass-loss event, which was interrupted ~ 5000 yr ago. Another possibility that should be considered is the interaction of the AGB stellar wind with the interstellar medium (ISM) resulting in a bow shock. Recently, Wareing et al. (2006) imaged the structure around R Hya with the *Spitzer*-telescope, revealing a one-sided parabolic arc $100''$ to the west, stretching from north to south. Using three-dimensional hydrodynamic simulations, they successfully modelled R Hya and its surroundings in terms of a bow shock into the surrounding ISM. Wareing et al. (2006) and Libert et al. (2007, considering the carbon star Y CVn) proposed this mechanism as another explanation of detached shells. The detached shell is then the result from the slowing-down of the stellar wind by surrounding matter.

3. Modelling the circumstellar envelope

The decline of the intensity of the CO vibration-rotation emission lines offers a strong diagnostic tool to study the circumstellar density structure within the first few hundred stellar radii. In Sect. 3.1, we therefore first elaborate on the constraints posed by the CO vibrational-rotational emission lines and compare the decline with an analytical solution computed under the assumption of a spherically symmetric, optically thin wind with a constant mass loss and constant expansion velocity. Thereafter, the CO vibration-rotation intensity decline in combination with the pure CO rotational line profiles will be modelled in detail using the non-LTE radiative transfer code GASTRoNOoM (Sect. 3.2).

3.1. Analytical solution

A simple analytical expression for the behaviour of the wavelength-integrated intensity as a function of the angular distance, β , can be constructed for a spherically symmetric and homogeneous wind. The wind is assumed to be optically thin in the CO lines along the line of sight, and has a constant mass-loss rate, \dot{M} , and a constant expansion velocity v_e . Under the assumption of a pure scattering process, Gustafsson et al. (1997) demonstrated that the ratio between the wavelength-integrated, line-scattered intensity $I_{\text{CO,lu}}$ ($\text{erg s}^{-1} \text{cm}^{-2} \text{arcsec}^{-2}$) received in a scattering line and the observed line-scattering stellar flux averaged across the line width, \bar{f}_λ ($\text{erg s}^{-1} \text{cm}^{-2} \text{cm}^{-1}$), can be written as

$$\frac{I_{\text{CO,lu}}(\beta)}{\bar{f}_\lambda} = \frac{206265}{32} \frac{e^2 \lambda^2}{m_e c^2} \frac{N_1(\text{CO})}{N(\text{CO})} \frac{\epsilon_{\text{CO}}}{v_e \mu m_{\text{H}}} f_{\text{lu}} \frac{\dot{M}}{D} \frac{1}{\beta^3}, \quad (1)$$

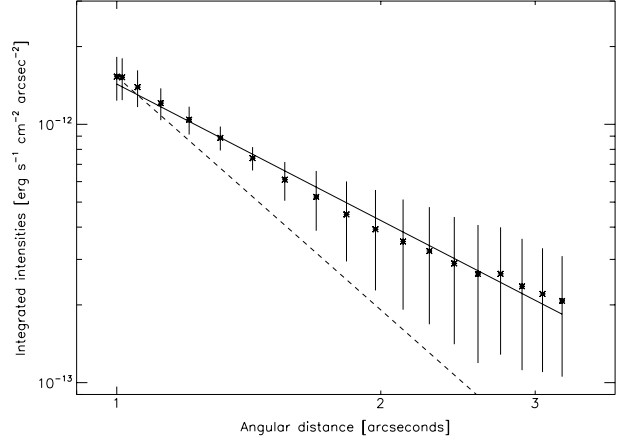


Fig. 11. Dependence of the mean of the scattered wavelength-integrated intensity of the circumstellar CO vibration-rotation lines on the angular distance on the sky, β . The full black line represents a $\beta^{-1.75}$ power law, the dashed line a β^{-3} power law.

where μ the mean molecular weight, D is the distance to the star from the Earth, β is the angular distance from the star to the scattering point on the sky in arcseconds, and f_{lu} the absorption oscillator strength of the line with l representing the lower level and u the upper level of the transition. Furthermore, ϵ_{CO} is the fractional abundance of CO relative to hydrogen, and $N_1(\text{CO})$ denotes the number density of CO molecules in the lower state l of the transition. Note that the number of scatterers per gram matter, n_{scat} , defined as

$$n_{\text{scat}} \equiv \frac{N_{\text{scat}}(r)}{\rho(r)} \quad (2)$$

is assumed to be independent of r , with $N_{\text{scat}}(r)$ the number of scattering particles per cm^3 and $\rho(r)$ the density. For the CO observations, n_{scat} can be written as

$$n_{\text{scat}} = \frac{N_1(\text{CO})}{N(\text{CO})} \frac{\epsilon_{\text{CO}}}{\mu m_{\text{H}}}. \quad (3)$$

Important in Eq. (1) is the β^{-3} dependence of the scattered wavelength-integrated intensity on the angular distance β . This dependence of the scattered intensity as a function of β is *not* confirmed by our observations: for the mean over all directions, we derive a much shallower decline, being $d \log I_{\text{CO}}/d \log \beta = -1.75$ (see Fig. 11)! For the different scan directions, the dependence of the intensity on the angular distance is illustrated in Fig. A.9, and is summarised in Table 2. The WS-data show the steepest intensity decline with $d \log I_{\text{CO}}/d \log \beta = -2.90$, while the NW-data only have a β -dependence of -1.21 . Optical depth effects and the violation of the assumptions of a homogeneous wind with constant mass-loss rate and constant expansion velocity will result in a dependence of the scattered intensity of the circumstellar rotation-vibration CO lines being different from the β^{-3} power law as derived in Eq. (1). Although within the standard deviation, the observational data in Fig. 11 show a “swing” around the line representing the $\beta^{-1.75}$ power law. This “swing” is well visible in the individual scan directions in Fig. A.9 (mainly the NW, SE, EN, WN, and WS-data), but levels out somewhat in the mean over all directions due to the fact that the “swing” is somewhat displaced in β for each of the scan directions, probably due to small displacements in the slit position. Clearly, this “swing” behaviour yields extra constraints on the circumstellar density structure not captured in the simple analytical expression derived in this section.

Table 2. Power-law dependence of the wavelength-integrated intensity I_{CO} on the angular distance β for the different scan directions.

Slit position	$d \log I_{\text{CO}} / d \log \beta$	Slit position	$d \log I_{\text{CO}} / d \log \beta$
NW	-1.2	WN	-1.7
NE	-1.5	EN	-2.5
SW	-2.3	WS	-2.9
SE	-1.5	ES	-2.6
Overall mean			-1.75

Ryde et al. (2000) derived a mean slope of the west, east, and north positions for the scattered CO vibra-rotational emission in the CSE of *o* Cet of $d \log I_{\text{CO}} / d \log \beta = -2.8$, with individual dependencies of the different scan directions ranging from -2.3 to -3.0 . Although not used in the analysis by Ryde & Schöier (2001), we note that also for *o* Cet a “swing” is visible around $3''$ from the star.

3.2. In-depth modelling of the vibration-rotation and pure rotation CO lines

3.2.1. GASTRoNOoM

The observed circumstellar (vibrational-) rotational CO lines provide information on the thermodynamical structure of the outflow of R Hya. For a proper interpretation of both data sets, we have used our theoretical non-LTE radiative transfer code GASTRoNOoM (Decin et al. 2006). The code first (1.) calculates the kinetic temperature in the shell by solving the equations of motion of gas and dust and the energy balance simultaneously; then (2.) solves the radiative transfer equation in the co-moving frame using the Approximate Newton-Raphson operator as developed by Schönberg & Hempe (1986) and computes the non-LTE level-populations consistently; and finally (3.) determines the observable line profile by ray-tracing. The main assumption of the code is a spherically symmetric wind, which is confirmed to be a good approximation in case of the CSE of R Hya by the IRAS-images shown by Hashimoto et al. (1998). The mass-loss rate is allowed to vary with radial distance from the star. For a full description of the code we refer to Decin et al. (2006). In the code, complete angular and frequency redistribution (CRD) is assumed. As described by Ryde & Schöier (2001), the assumption of CRD is valid for the pure rotational CO transitions, since the collisions will have time to reset the frequency-memory of the excited atoms. For the vibrational-rotational CO transitions, this assumption can be problematic since the spontaneous de-excitation rates are of the order of 10 s^{-1} . However, Ryde & Schöier (2001) demonstrated that for the low mass-loss rate models and the low optical depths occurring in the CSEs of stars, such as *o* Cet, and similarly of R Hya, the assumption of CRD is justified.

As explained in Sect. 2.2, the pure rotational CO line profiles show quite large differences in their absolute intensity level (after correction for different telescope size and HPBW) between the various observations of the same rotational transition, although the line shapes are similar. Decin et al. (2006) demonstrated that not only the integrated line intensities, but particularly the line shapes should be taken into account for a proper determination of the mass-loss history. To find the best-fit model and derive a 95% confidence interval for the model parameters, we will use the log-likelihood-method as developed in Decin et al. (2007). This method gives a greater weight to the line shapes than to the integrated line intensity. It turned out to be impossible to find a model structure for the envelope fulfilling

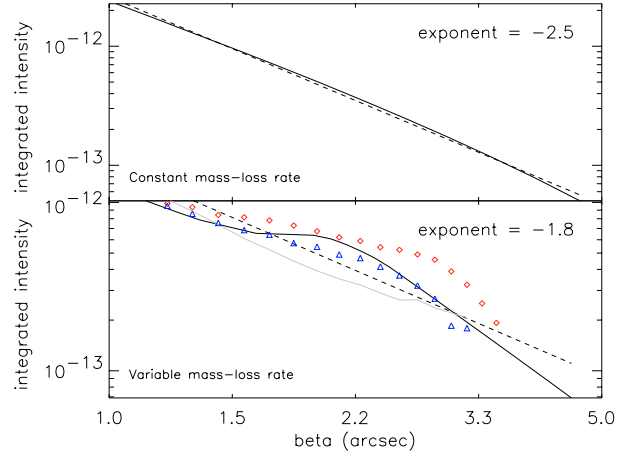


Fig. 12. Decline of the theoretically predicted integrated intensity (in $\text{erg s}^{-1} \text{cm}^{-2} \text{arcsec}^{-2}$) of the circumstellar CO vibration-rotation emission as a function of angular distance β from the star. The full black line represents the GASTRoNOoM-predictions, the dashed black line represents the best-fit power law ($I \propto \beta^a$), with the exponent a specified in each panel. *Upper panel:* adopting a constant mass-loss rate, with same parameters as in Fig. 10. *Lower panel:* the best-fit model having a variable mass-loss rate with parameters as listed in Table 3. The grey line represents the decline of the overall mean of the data, the triangles show the behaviour in the NE-direction, and the diamonds that in the NW-direction.

the absolute flux criteria of all pure rotational CO lines (listed in Table 1) due to the large internal absolute flux differences. We therefore have opted to increase the absolute flux uncertainty to 40% on the IRAM and JCMT-data. Note that the log-likelihood method also accounts for the rms-noise on the data.

3.2.2. Results

As shown in Fig. 10 a model with a constant mass-loss rate fits quite nicely the integrated intensities of the pure rotational line profiles, although the line shapes are not well reproduced. In addition, the theoretically predicted wavelength-integrated scattered line intensities of the CO vibration-rotation emission lines show a $\beta^{-2.5}$ -dependency (see Fig. 12), being too steep and failing to reproduce the observed “swing”. To illustrate the sensitivity of the intensity decline to the mass-loss rate, an increase of \dot{M} from $5 \times 10^{-8} M_{\odot}/\text{yr}$ to $1 \times 10^{-6} M_{\odot}/\text{yr}$ results in the integrated CO intensity being well represented by a β^a power-law, with the exponent a rising from -2.7 to -2.2 . However, no “swing” is predicted.

Using the statistical method outlined in Decin et al. (2007), a grid of $\sim 400\,000$ models was computed to find the best-fit model to both the pure rotational and vibrational-rotational CO lines. This grid should constrain the mass-loss history of R Hya. The grid was constructed around the stellar parameters as deduced and discussed by Zijlstra et al. (2002): an effective temperature T_{eff} of 2830 K; a stellar mass of $2 M_{\odot}$; a luminosity L of $1.16 \times 10^4 L_{\odot}$; and a radius R of $450 R_{\odot}$ ($=3.1 \times 10^{13} \text{ cm}$). Mass-loss rate values ranged between $1 \times 10^{-8} M_{\odot}/\text{yr}$ and $5 \times 10^{-6} M_{\odot}/\text{yr}$, being either constant throughout the envelope or showing variations with amplitudes between a factor of 2 and 100. In case of a constant mass-loss rate, the value of the outer photodissociation radius, R_{outer} , is set at the radius where the CO abundance drops to 1% of its value at the photosphere, using the photodissociation results of Mamon et al. (1988). In the case of variations in the mass-loss rate, R_{outer} is a free parameter

Table 3. Parameters of the model with best goodness-of-fit for R Hya. In the second column the values of the best-fit model parameters are listed, in the third column the confidence interval around the parameter is specified. The numbers in italics are input parameters that have been kept fixed at the given values.

Parameter	Value	Confidence interval
T_{eff} [K]	2830	2400–2900
R_{\star} [10^{13} cm]	3.1	2.5–3.1
L_{\star} [$10^4 L_{\odot}$]	1.16	0.5–1.3
$\varepsilon(\text{C})$ [10^{-4}]	3	–
$\varepsilon(\text{O})$ [10^{-4}]	8.5	–
distance [pc]	165	165–180
R_{inner} [R_{\star}]	150	130–240
R_{outer} [R_{\star}]	2350	2000–8000
v_{∞} [km s^{-1}]	8	8–9
$\dot{M}(r)$ [$M_{\odot} \text{ yr}^{-1}$]	$\sim 1 \times 10^{-8}$ ($\sim 1\text{--}150 R_{\star}$)	$.8\text{--}1.2 \times 10^{-8}$
	$\sim 2 \times 10^{-7}$ ($\sim 150\text{--}5000 R_{\star}$)	$1\text{--}2.2 \times 10^{-7}$

in the theoretical code with the constraint that R_{outer} should be smaller than the R_{outer} -value obtained using the formula of Mamon et al. (1988) for a value of the mass-loss rate equal to that at the outermost radius point (see the discussion in Decin et al. 2007).

When checking the decline of the scattered wavelength-integrated intensities of the CO vibration-rotation emission lines, it turned out that only a step in \dot{M} can reproduce the “swing” visible in the observations. In case only the CO pure rotational lines would have been at our disposal, it would have been impossible to remove the degeneracy in models constraining the inner 3'' region of the envelope.

Parameters characterising the CSE of the model with the best goodness-of-fit are listed in Table 3. The derived temperature profile, velocity structure, and mass-loss history are displayed in Fig. 13; a comparison between the observed rotational CO lines and theoretical predictions is shown in Fig. 10; and the decline of the integrated intensity of the CO vibrational-rotational emission lines is displayed in Fig. 12. The 95% confidence intervals around T_{eff} , R_{\star} , L_{\star} , R_{outer} , \dot{M} , and the distance to the star are determined from the modelling of the pure rotational CO lines, while the vibrational-rotational CO lines constrain the confidence intervals of R_{inner} and the amplitude of the jump in \dot{M} around $150 R_{\star}$. The derived confidence intervals are statistical uncertainties, which should be interpreted in the light of the model assumptions of a spherically symmetric wind with a monotonically increasing velocity structure.

The photodissociation radius calculated using the formula of Mamon et al. (1988) for $\dot{M} = 2 \times 10^{-7} M_{\odot}/\text{yr}$ and $v_{\infty} = 8 \text{ km s}^{-1}$ is $\sim 2350 R_{\star}$. Mainly the CO $J = 1\text{--}0$ line is influenced by the outer radius. Due to the suspected large absolute calibration uncertainty for the IRAM CO $J = 1\text{--}0$ line of R Hya and the IRAM *HPBW* of 23'' ($\sim 1850 R_{\star}$), the outer radius is only loosely constrained. Moreover, it is unclear how the bow shock, as detected by Wareing et al. (2006) around 100'' ($\sim 8000 R_{\star}$) influences the CO-photodissociation radius and the density structure in the outer envelope. The log-likelihood tests yield acceptable R_{outer} -values between 2000 and 8000 R_{\star} . The small differences between the log-likelihood values of the best-fit model and the model with $R_{\text{outer}} = 8000 R_{\star}$ are due to the (very) small CO abundance for $r > 2300 R_{\star}$. The gas temperature at $2000 R_{\star}$ is still quite high and estimated to be around 180 K; at $8000 R_{\star}$, the gas temperature is around 50 K.

Our best-fit model has an inner radius R_{inner} of $150 R_{\star}$, representing the inner radius of a detached envelope in which the

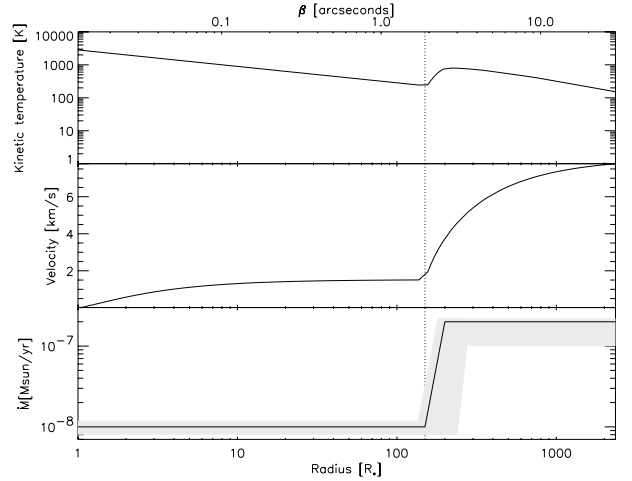


Fig. 13. Upper: estimated temperature profile, middle: estimated velocity structure, and bottom: estimated mass-loss rate $\dot{M}(r)$ for R Hya as a function of radial distance to the star (black line). The shading region in the bottom panel displays the confidence intervals of the estimated mass-loss parameters. The dashed line indicates R_{inner} .

dust condensed much closer to the star. This is in nice agreement with the results of a detached dust shell by Zijlstra et al. (2002) and Hashimoto et al. (1998). In the theoretical model, R_{inner} the gas kinetic temperature and velocity structure beyond R_{inner} are computed by solving simultaneously the equations of motion of gas and dust and the energy balance. The temperature structure between R_{\star} and R_{inner} is described using a power law ($T(r) \propto r^{(-0.5)}$), which holds when both emission and absorption are optically thin (see Fig. 13); the velocity law in this inner region is approximated by the classical β -law (Decin et al. 2006). The region between R_{\star} and R_{inner} is the so-called “quasi-stationary” layer, where molecules can reside at low expansion velocity, and (almost) no dust is present to drive the wind. Possible reasons for the change in dust mass, and hence mass-loss rate, at R_{inner} are further discussed in Sect. 4. Slightly beyond R_{inner} , the temperature increases due to gas-grain collisional heating. Further outwards, the energy balance is determined by the adiabatic expansion of the gas.

Inspecting Fig. 10, we see a nice resemblance between the observed rotational CO line profile shapes and the model predictions. Note that if the displayed IRAM profiles would have been in terms of the antenna temperature, the corrected main-beam temperature would perfectly match the model predictions. A clear asymmetry is visible in all radio CO line profiles. Quite often, this kind of asymmetry is explained in terms of self-absorption along the line of sight (e.g. Ryde & Schöier 2001), although an asymmetric stellar atmosphere, unresolved bright spots or asymmetries in the CSE-structure may explain this behaviour. Moreover, it is unclear how the downstream of the detected bow shock around R Hya at $\sim 100''$ influences the circumstellar structure closer to the target.

The decline of the integrated intensity of the vibra-rotational CO emission lines as a function of the angular distance from the star is also reproduced quite well (see Fig. 12). Since the “swing” is somewhat canceled in the mean over all directions (grey line), likely due to variations in the exact slit position, the NE and NW-directions are also plotted to illustrate the strength of the “swing”-behaviour. Furthermore, comparing the full vibrational CO R(1), R(2), and R(3) line profiles (i.e., not only the integrated intensities) for the 38 sub-spectra extracted from each of the off-star data sets corroborates the quality of our

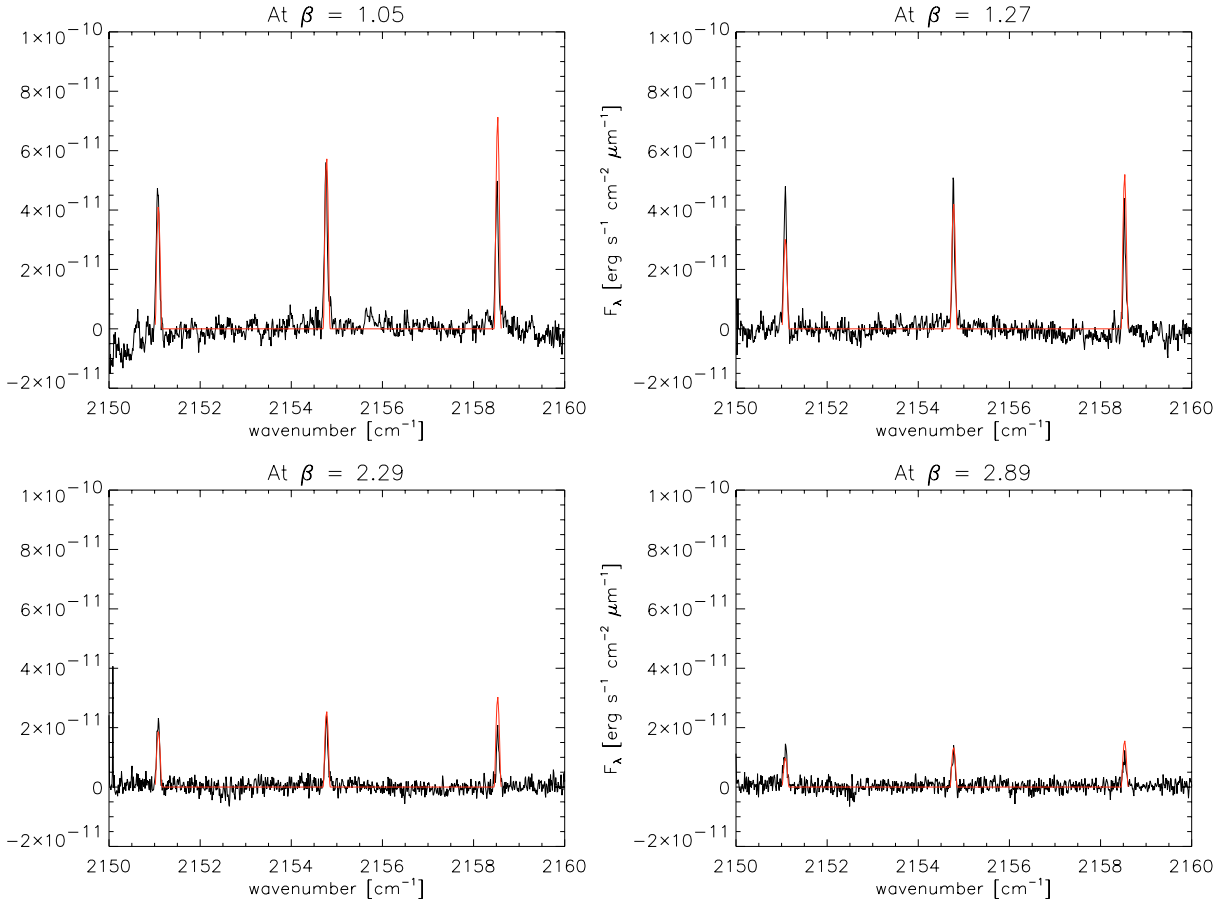


Fig. 14. The CO vibra-rotational R(1), R(2), R(3) lines observed at different angular distance from the star (black) are compared with the theoretical model predictions (red) for the best-fit model with parameters as specified in Table 3. The displayed off-star data are for data set 128 (EW-slit N1 E2.5).

best-fit theoretical model (see Fig. 14): at different angular distances from the star, the observed and theoretically predicted line strengths of the three CO vibra-rotational lines match nicely.

In addition, using the GASTRoNOoM-code, the Phoenix observations, done with the 4 m Mayall telescope at Kitt Peak by Ryde et al. (2000) for σ Cet, have been simulated using the stellar parameters and mass-loss rate history as derived by Ryde & Schöier (2001). Using their “cavity” model, with an inner radius at $\sim 50 R_{\star}$ (or $\sim 1''$), we obtain a β -dependence for the decline of the wavelength-integrated intensity of the circumstellar CO vibration-rotation emission of $d \log I_{\text{CO}}/d \log \beta = -2.4$. No “swing” is predicted, since the inner radius lies within the geometrical region traced by the scattered light (i.e. being from $2''$ to $7''$).

4. Discussion

It is evident that the modelling of the pure rotational CO emission lines *in combination with* the scattered vibrational-rotational low-excitation CO transitions has a strong diagnostic power for probing the temperature, density, and velocity structure of the CSE of R Hya, and, therefore, for studying the mass-loss history of this Mira-variable. The main result from our in-depth analysis is that the mass-loss rate of R Hya has changed at about $150 R_{\star}$ from the star (at $\sim 1.9''$ or ~ 220 yr ago for an expansion velocity of 8 km s^{-1}) with a factor of ~ 20 . The change of the mass-loss rate as a function of time agrees with the predictions of Zijlstra et al. (2002) who analysed the period evolution

of R Hya. They showed that the period of R Hya decreased linearly between AD 1770 and 1950, and has stabilised at 385 d since 1950. From fitting the SED, Zijlstra et al. (2002) concluded that the mass-loss rate should have changed with at least a factor of 10, while Hashimoto et al. (1998) suggested that the SED and IRAS-images should be interpreted in terms of a detached shell. The presence of an SiO maser (Snyder & Buhl 1975), however, proves that the mass-loss rate has not ceased completely. As demonstrated by Zijlstra et al. (2002) the evolution of the mass-loss rate as a function of period agrees with the mass-loss formalism of Vassiliadis & Wood (1993), but is much larger than predicted by Blöcker (1995).

We realize that a disadvantage of our analysis method of R Hya is that the star is not allowed to *evolve*, in the sense that the luminosity, effective temperature and stellar radius are kept constant for the computation of the structure of the whole envelope. The gradual change in period of R Hya implies that its pulsation mode has remained constant, and that its evolution is related to a change in stellar parameters. As discussed by Zijlstra et al. (2002) various relations (such as the period-luminosity relation, evolutionary tracks, colour-period relation, T_{eff} -colour relation) are not mutually consistent. A luminosity decrease of R Hya in the last 340 years is possible, but not proven. Only a decrease in radius by 14–18%, obtained from the period, appears well constrained.

The declining period of R Hya between AD 1770 and 1950 has been attributed by Wood & Zarro (1981) to a possible recent thermal pulse. Wood & Zarro (1981) argued that R Hya

is presently in the luminosity decline following the peak of the pulse, with the peak luminosity around AD 1750. The analysis of Zijlstra et al. (2002) places the peak luminosity plateau around AD 1700. Since the detached shell with inner radius of 1–2 arcmin found in the 60 μm IRAS images by Hashimoto et al. (1998) can be interpreted in terms of an AGB-ISM bow shock (Wareing et al. 2006) and no mass-loss variation around 1–2 arcmin from the star needs to be invoked, the thermal-pulse model is capable of explaining the full mass-loss history of R Hya. However, other causes, such as envelope relaxation due to the non-linear pulsations (Zijlstra et al. 2002), hydrodynamical oscillations due to instabilities in the gas-dust coupling in the CSE while the star is on the AGB (Simis et al. 2001) or a solar-like magnetic activity cycle in the progenitor AGB star (Soker 2000), cannot be ruled out.

5. Conclusions

For the first time, both the CO pure rotational emission line profiles ($J=1-0$ through $J=6-5$) and the CO vibrational-rotational scattered resonance lines from the fundamental band of the unusual Mira variable R Hya are analysed in detail using a non-LTE radiative transfer code. The dependency of the CO vibra-rotational emission on the angular distance on the sky clearly points towards a *variation in the mass-loss rate* at $\sim 1.9''$ from the star. An in-depth analysis of the CO pure rotational emission line profiles and the vibra-rotational circumstellar CO emission provides evidence for a drop in mass-loss rate some 220 yr ago with a factor ~ 20 . This change in mass-loss rate coincides with a period decline between AD 1770 and 1950, corroborating the analysis of Zijlstra et al. (2002) and Wood & Zarro (1981) that a He-flash may be the cause of the period decline. A second mass-loss event originally suggested by IRAS-images (Hashimoto et al. 1998; Zijlstra et al. 2002) may not be due to a change in mass-loss rate, but may be caused by the AGB-ISM bow shock, detected in 2006 by Wareing et al. (2006).

The results point toward a mass-loss history during the last ~ 2000 yr with a constant \dot{M} of $\sim 2 \times 10^{-7} M_{\odot}/\text{yr}$ until ~ 220 yr ago, at which moment a He-flash altered the internal stellar structure, resulting in a decrease of \dot{M} by a factor ~ 20 . The period evolution, SED, and circumstellar CO pure-rotational and vibra-rotational emission lines of R Hya can be explained by this mass-loss history.

Acknowledgements. The observations are based on observations obtained at the Gemini Observatory, which is operated by the Association of Universities for Research in Astronomy, Inc., under a cooperative agreement with the NSF on behalf of the Gemini partnership: the National Science Foundation (US), the Science and Technology Facilities Council (UK), the National Research Council (Canada), CONICYT (Chile), the Australian Research Council (Australia), CNPq (Brazil) and SECYT (Argentina). The observations were obtained with the Phoenix infrared spectrograph, which was developed and is operated by the National Optical Astronomy Observatory. The spectra were obtained as part of program GS-2005A-C-8.

L.D. and M.R. acknowledge financial support from the Fund for Scientific Research – Flanders (Belgium). N.R. is Royal Swedish Academy of Sciences Research Fellow supported by a grant from the Knut and Alice Wallenberg

Foundation. The computations for this research have been done on the VIC HPC Cluster of the KULeuven. We are grateful to the LUDIT HPC team for their support. We would like to thank Remo Tilanus (JCMT) for his support during the observations and reduction of the data. Prof. J. R. Knapp and Dr. D. Teyssier are thanked for providing us the rotational CO emission profiles of R Hya obtained with the CSO and IRAM.

References

- Aringer, B., Kerschbaum, F., & Jørgensen, U. G. 2002, A&A, 395, 915
 Blöcker, T. 1995, A&A, 297, 727
 Bujarrabal, V., Fuente, A., & Omont, A. 1994, A&A, 285, 247
 Decin, L., & Eriksson, K. 2007, A&A, 472, 1041
 Decin, L., Hony, S., de Koter, A., et al. 2006, A&A, 456, 549
 Decin, L., Hony, S., de Koter, A., et al. 2007, A&A, 475, 233
 Goorvitch, D., & Chackerian, C. 1994, ApJS, 91, 483
 Gustafsson, B., Bell, R. A., Eriksson, K., & Nordlund, A. 1975, A&A, 42, 407
 Gustafsson, B., Eriksson, K., Kiselman, D., Olander, N., & Olofsson, H. 1997, A&A, 318, 535
 Habing, H. J. 1996, A&A Rev., 7, 97
 Hashimoto, O., Nakada, Y., Onaka, T., Tanabe, T., & Kamijo, F. 1990, in *Dusty Objects in the Universe*, ed. E. Bussoletti, & A. A. Vittone, Astrophys. Space Sci. Library, 165, 95
 Hashimoto, O., Izumiura, H., Kester, D. J. M., & Bontekoe, T. R. 1998, A&A, 329, 213
 Hinkle, K. H., Cuberly, R. W., Gaughan, N. A., et al. 1998, in *Infrared Astronomical Instrumentation*, ed. A. M. Fowler, Proc. SPIE, 3354, 810
 Huggins, P. J., & Healy, A. P. 1986, ApJ, 304, 418
 Jones, H. R. A., Pavlenko, Y., Viti, S., & Tennyson, J. 2003, in *The Future of Cool-Star Astrophysics: 12th Cambridge Workshop on Cool Stars, Stellar Systems, and the Sun (2001 July 30–August 3)*, ed. A. Brown, G. M. Harper, & T. R. Ayres (University of Colorado), 12, 899
 Jørgensen, U. G., Jensen, P., Sørensen, G. O., & Aringer, B. 2001, A&A, 372, 249
 Kemper, F., Stark, R., Justtanont, K., et al. 2003, A&A, 407, 609
 Knapp, G. R., Phillips, T. G., & Huggins, P. J. 1980, ApJ, 242, L25
 Knapp, G. R., Young, K., Lee, E., & Jorissen, A. 1998, ApJS, 117, 209
 Libert, Y., Gérard, E., & Le Bertre, T. 2007, MNRAS, 380, 1161
 Little, S. J., Little-Marenin, I. R., & Bauer, W. H. 1987, AJ, 94, 981
 Mamon, G. A., Glassgold, A. E., & Huggins, P. J. 1988, ApJ, 328, 797
 Morris, M. 1975, ApJ, 197, 603
 Morris, M. 1980, ApJ, 236, 823
 Olmon, F. M., Raimond, E., Neugebauer, G., et al. 1986, A&AS, 65, 607
 Partridge, H., & Schwenke, D. W. 1997, J. Chem. Phys., 106, 4618
 Plez, B., & Lambert, D. L. 1994, ApJ, 425, L101
 Roddier, F. 1981, in *Progress in optics* (Amsterdam: North-Holland Publishing Co.), 19, 281
 Ryde, N., & Schöier, F. L. 2001, ApJ, 547, 384
 Ryde, N., Gustafsson, B., Eriksson, K., & Hinkle, K. H. 2000, ApJ, 545, 945
 Schöier, F. L., Olofsson, H., & Lundgren, A. A. 2006, A&A, 454, 247
 Schönberg, K., & Hempe, K. 1986, A&A, 163, 151
 Simis, Y. J. W., Icke, V., & Dominik, C. 2001, A&A, 371, 205
 Smith, B. J., Leisawitz, D., Castelar, M. W., & Luttermoser, D. 2002, AJ, 123, 948
 Snyder, L. E., & Buhl, D. 1975, ApJ, 197, 329
 Soker, N. 2000, ApJ, 540, 436
 Teyssier, D., Hernandez, R., Bujarrabal, V., Yoshida, H., & Phillips, T. G. 2006, A&A, 450, 167
 Vassiliadis, E., & Wood, P. R. 1993, ApJ, 413, 641
 Wannier, P. G., & Sahai, R. 1986, ApJ, 311, 335
 Wareing, C. J., Zijlstra, A. A., Speck, A. K., et al. 2006, MNRAS, 372, L63
 Winters, J. M., Le Bertre, T., Jeong, K. S., Nyman, L.-Å., & Epchtein, N. 2003, A&A, 409, 715
 Wood, P. R., & Zarro, D. M. 1981, ApJ, 247, 247
 Young, K., Phillips, T. G., & Knapp, G. R. 1993, ApJ, 409, 725
 Zijlstra, A. A., Bedding, T. R., & Mattei, J. A. 2002, MNRAS, 334, 498
 Zuckermann, B., Palmer, P., Morris, M., et al. 1977, ApJ, 211, L97

Appendix A: CO vibrational-rotational transitions of R Hya: logbook and figures

The logbook and extra figures of the CO vibrational-rotational lines excited in the CSE around R Hya are given in this appendix.

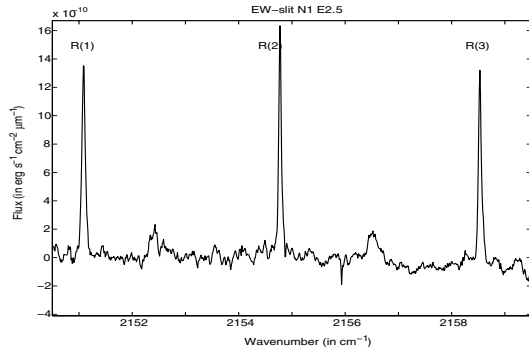
Table [A.1](#) describes the logbook of the Phoenix CO vibrational-rotational transitions imaging the CSE of R Hya. Figures [A.1–A.4](#) display the circumstellar CO vibration-rotation R(1), R(2), and R(3) emission lines integrated over the slit for the 16 off-star observations of R Hya. Inspecting Fig. [A.3](#), it is clear that the CO emission lines in data sets (158, 161) are a factor 2 higher than in data sets (141, 142).

The decline of the intensity of the circumstellar CO emission as a function of the angular distance β in the south, east and west position is given in Figs. [A.5–A.7](#), respectively. Omitting data sets (149, 150) in the westward scans in the CSE of R Hya yield a better overlap between the mean of the WS and SW scans, as illustrated in Fig. [A.8](#) (we refer to the paper for a discussion on this topic).

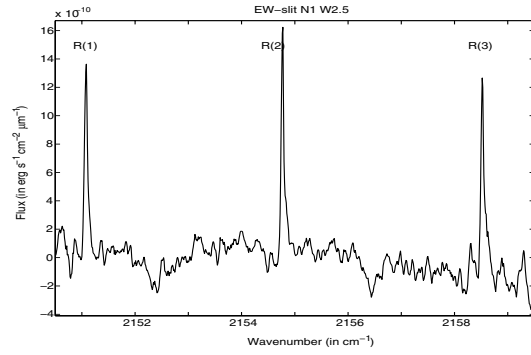
Figure [A.9](#) displays the dependence of the scattered wavelength-integrated intensities of the 3 CO vibration-rotation lines as a function of the angular distance for the different scan directions, together with the best-fit power law to the data.

Table A.1. Logbook of the CO vibrational-rotational Phoenix observations of R Hya. A notation “EW-slit N1 E2.5” indicates a slit-position oriented in the east-west direction, which is 1” offset to the north from the star and which has been moved 2.5” in the east-direction along the slit. For the off-star observations, the number of the data we used is also listed in the first column. β Ori is a telluric reference star; the observations of α Vir are used to compute the slit loss (see the paper for more details).

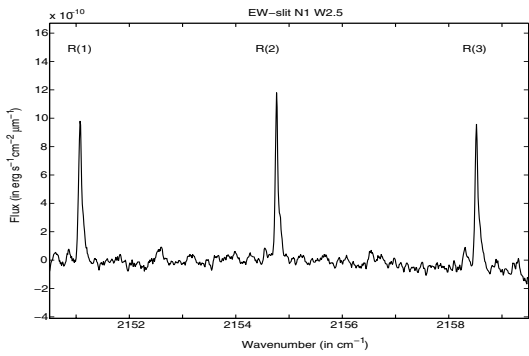
Observation – data set	Date and hour (UTC)	Airmass	Exposure time	Slit position
flat	26/02/2005 23h46m17s		20 s	
flat	26/02/2005 23h48m02s		20 s	
flat	26/02/2005 23h48m02s		20 s	
flat	26/02/2005 23h48m02s		20 s	
flat	26/02/2005 23h48m02s		20 s	
flat	26/02/2005 23h48m02s		20 s	
flat	26/02/2005 23h48m02s		20 s	
flat	26/02/2005 23h48m02s		20 s	
flat	26/02/2005 23h48m02s		20 s	
flat	26/02/2005 23h48m02s		20 s	
dark	26/02/2005 23h56m40s		20 s	
dark	26/02/2005 23h56m40s		20 s	
dark	26/02/2005 23h56m40s		20 s	
dark	26/02/2005 23h56m40s		20 s	
dark	26/02/2005 23h56m40s		20 s	
dark	26/02/2005 23h56m40s		20 s	
dark	26/02/2005 23h56m40s		20 s	
dark	26/02/2005 23h56m40s		20 s	
dark	26/02/2005 23h56m40s		20 s	
dark	26/02/2005 23h56m40s		20 s	
dark	26/02/2005 23h56m40s		20 s	
dark	26/02/2005 23h56m40s		20 s	
beta Ori	27/02/2005 00h44m53s	1.133	20 s	on-star
beta Ori	27/02/2005 00h46m51s	1.136	20 s	on-star
beta Ori	27/02/2005 00h48m41s	1.139	20 s	on-star
beta Ori	27/02/2005 00h50m40s	1.142	20 s	on-star
R Hydrae – data set 108	27/02/2005 05h50m11s	1.115	1 s	on-star
R Hydrae – data set 109	27/02/2005 05h50m52s	1.113	1 s	on-star
R Hydrae – data set 110	27/02/2005 05h51m25s	1.112	1 s	on-star
R Hydrae – data set 111	27/02/2005 05h52m06s	1.111	1 s	on-star
R Hydrae – data set 112	27/02/2005 05h53m28s	1.108	30 s	EW-slit N1 E2.5
R Hydrae – data set 113	27/02/2005 05h56m56s	1.101	30 s	EW-slit N1 W2.5
sky	27/02/2005 06h00m28s	1.095	30 s	EW-slit N15 W2.5
sky	27/02/2005 06h03m06s	1.090	30 s	EW-slit N15 W2.5
R Hydrae – data set 116	27/02/2005 06h06m33s	1.084	30 s	EW-slit S1 W2.5
R Hydrae – data set 117	27/02/2005 06h09m58s	1.079	30 s	EW-slit S1 E2.5
sky	27/02/2005 06h13m36s	1.073	30 s	EW-slit S15 E2.5
sky	27/02/2005 06h16m11s	1.069	30 s	EW-slit S15 E2.5
R Hydrae – data set 123	27/02/2005 06h30m09s	1.050	30 s	EW-slit S1 E2.5
R Hydrae – data set 124	27/02/2005 06h33m39s	1.046	30 s	EW-slit S1 W2.5
sky	27/02/2005 06h37m17s	1.042	30 s	EW-slit S15 W2.5
sky	27/02/2005 06h39m52s	1.039	30 s	EW-slit S15 W2.5
R Hydrae – data set 127	27/02/2005 06h43m44s	1.036	30 s	EW-slit N1 W2.5
R Hydrae – data set 128	27/02/2005 06h47m45s	1.032	30 s	EW-slit N1 E2.5
sky	27/02/2005 06h51m07s	1.029	30 s	EW-slit N15 E2.5
sky	27/02/2005 06h53m45s	1.027	30 s	EW-slit N15 E2.5
R Hydrae – data set 137	27/02/2005 07h29m32s	1.009	1 s	on-star
R Hydrae – data set 138	27/02/2005 07h30m12s	1.009	1 s	on-star
R Hydrae – data set 139	27/02/2005 07h30m46s	1.009	1 s	on-star
R Hydrae – data set 140	27/02/2005 07h31m27s	1.008	1 s	on-star
R Hydrae – data set 141	27/02/2005 07h33m20s	1.008	30 s	NS-slit E1 N2.5
R Hydrae – data set 142	27/02/2005 07h36m43s	1.008	30 s	NS-slit E1 S2.5
sky	27/02/2005 07h41m19s	1.007	30 s	NS-slit E15 S2.5
sky	27/02/2005 07h44m09s	1.007	30 s	NS-slit E15 S2.5
R Hydrae – data set 149	27/02/2005 07h59m14s	1.009	30 s	NS-slit W1 N2.5
R Hydrae – data set 150	27/02/2005 08h02m53s	1.010	30 s	NS-slit W1 S2.5
sky	27/02/2005 08h06m25s	1.011	30 s	NS-slit W15 S2.5
sky	27/02/2005 08h09m01s	1.012	30 s	NS-slit W15 S2.5
R Hydrae – data set 158	27/02/2005 08h28m17s	1.022	30 s	NS-slit E1 N0
R Hydrae – data set 159	27/02/2005 08h31m25s	1.025	30 s	NS-slit W1 N0
R Hydrae – data set 160	27/02/2005 08h34m11s	1.027	30 s	NS-slit W1 N0
R Hydrae – data set 161	27/02/2005 08h37m47s	1.030	30 s	NS-slit E1 N0
sky	27/02/2005 08h41m29s	1.033	30 s	NS-slit E15 S0
sky	27/02/2005 08h44m05s	1.035	30 s	NS-slit E15 S0
sky	27/02/2005 08h46m55s	1.038	30 s	NS-slit E15 S0
alpha Vir	27/02/2005 09h23m57s	1.164	1 s	on-star
alpha Vir	27/02/2005 09h31m14s	1.181	1 s	on-star no slit
alpha Vir	27/02/2005 09h31m54s	1.182	1 s	on-star no slit
alpha Vir	27/02/2005 09h32m28s	1.184	1 s	on-star no slit
alpha Vir	27/02/2005 09h33m10s	1.185	1 s	on-star no slit



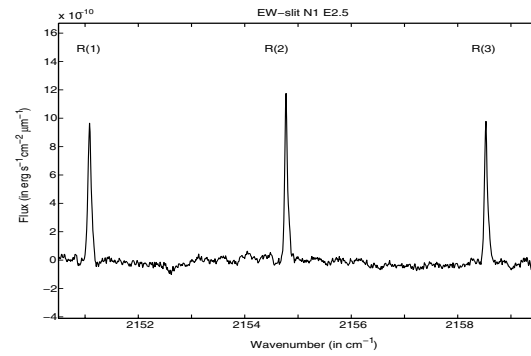
(a) The CO emission lines of data set 112, being a EW-slit N1 E2.5.



(b) The CO emission lines of data set 113, being a EW-slit N1 W2.5.

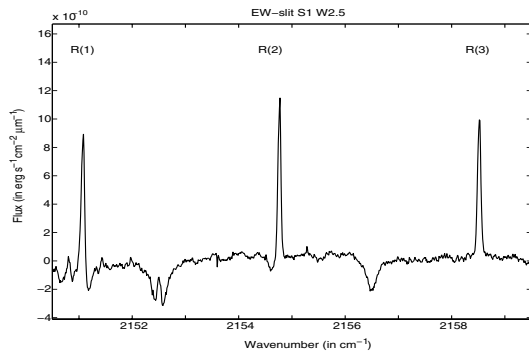


(c) The CO emission lines of data set 127, being a EW-slit N1 W2.5.

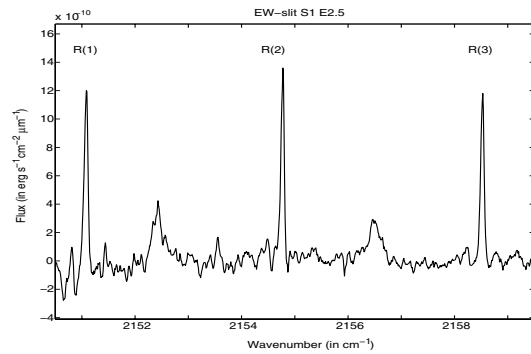


(d) The CO emission lines of data set 128, being a EW-slit N1 E2.5.

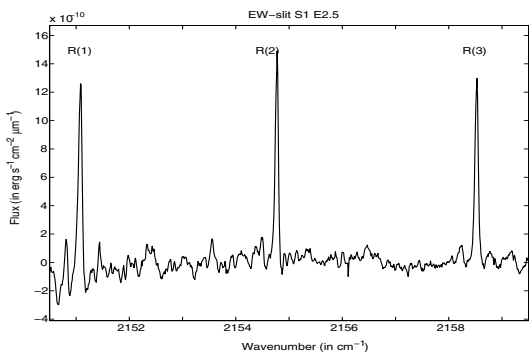
Fig. A.1. The CO vibration-rotation emission lines north of R Hydrae, integrated over the slit.



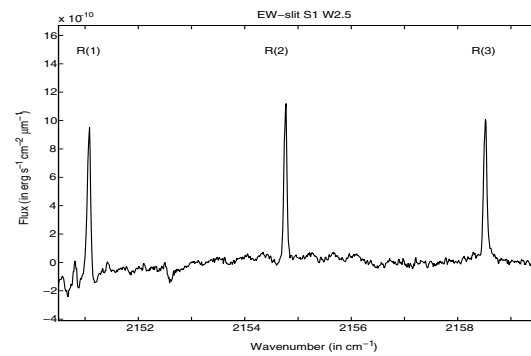
(a) The CO emission lines of data set 116, being a EW-slit S1 W2.5.



(b) The CO emission lines of data set 117, being a EW-slit S1 E2.5.

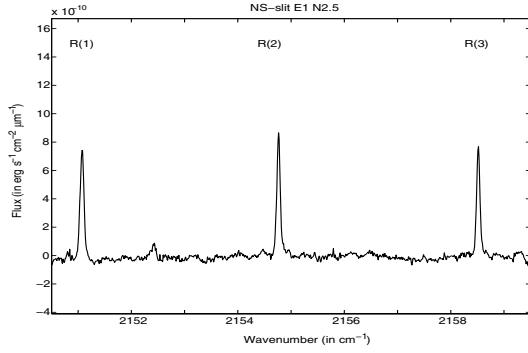


(c) The CO emission lines of data set 123, being a EW-slit S1 E2.5.

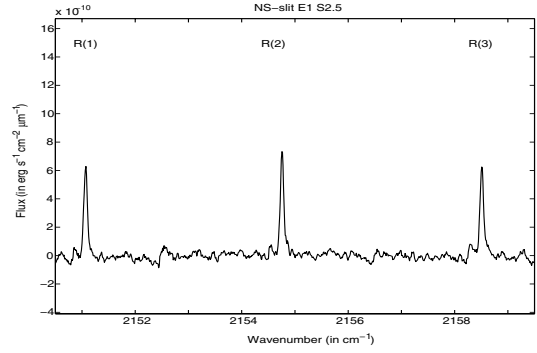


(d) The CO emission lines of data set 124, being a EW-slit S1 W2.5.

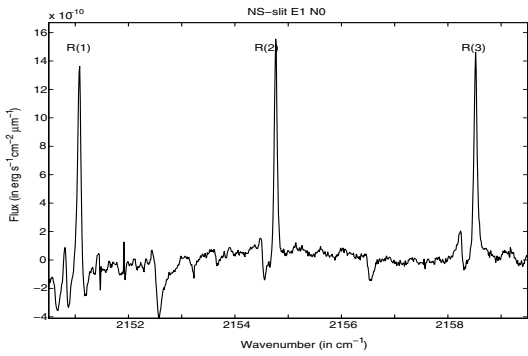
Fig. A.2. The CO vibration-rotation emission lines south of R Hydrae, integrated over the slit.



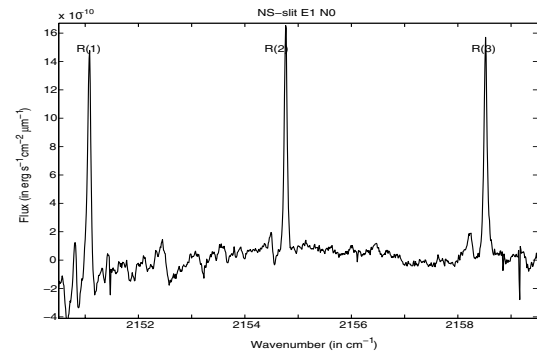
(a) The CO emission lines of data set 141, being a NS-slit E1 N2.5.



(b) The CO emission lines of data set 142, being a NS-slit E1 S2.5.

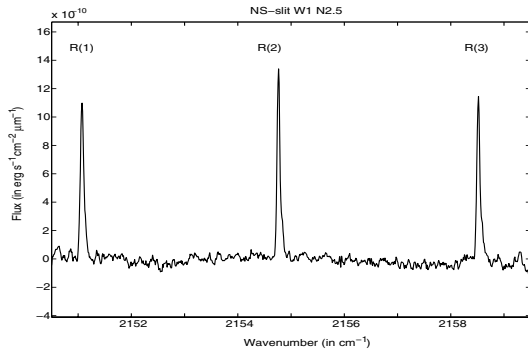


(c) The CO emission lines of data set 158, being a NS-slit E1 N0.

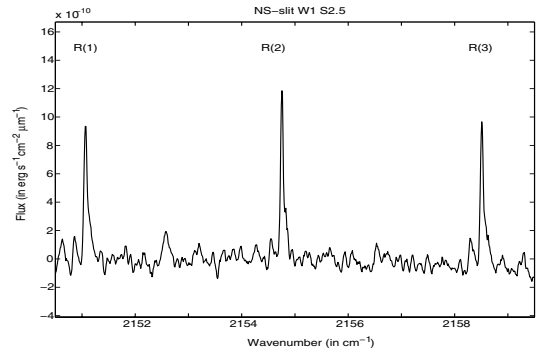


(d) The CO emission lines of data set 161, being a NS-slit E1 N0.

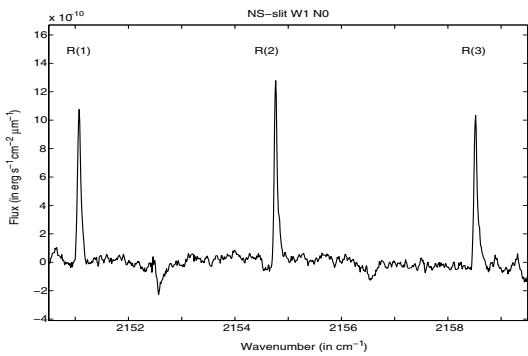
Fig. A.3. The CO vibration-rotation emission lines east of R Hydrae, integrated over the slit.



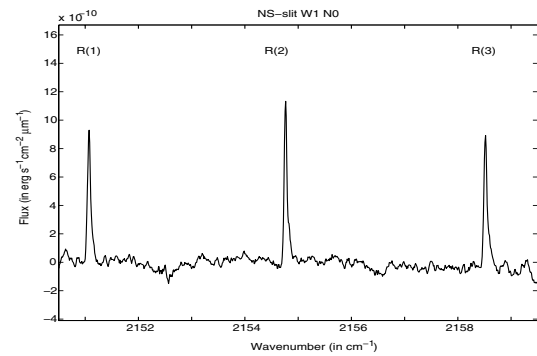
(a) The CO emission lines of data set 149, being a NS-slit W1 N2.5.



(b) The CO emission lines of data set 150, being a NS-slit W1 S2.5.



(c) The CO emission lines of data set 159, being a NS-slit W1 N0.



(d) The CO emission lines of data set 160, being a NS-slit W1 N0.

Fig. A.4. The CO vibration-rotation emission lines west of R Hydrae, integrated over the slit.

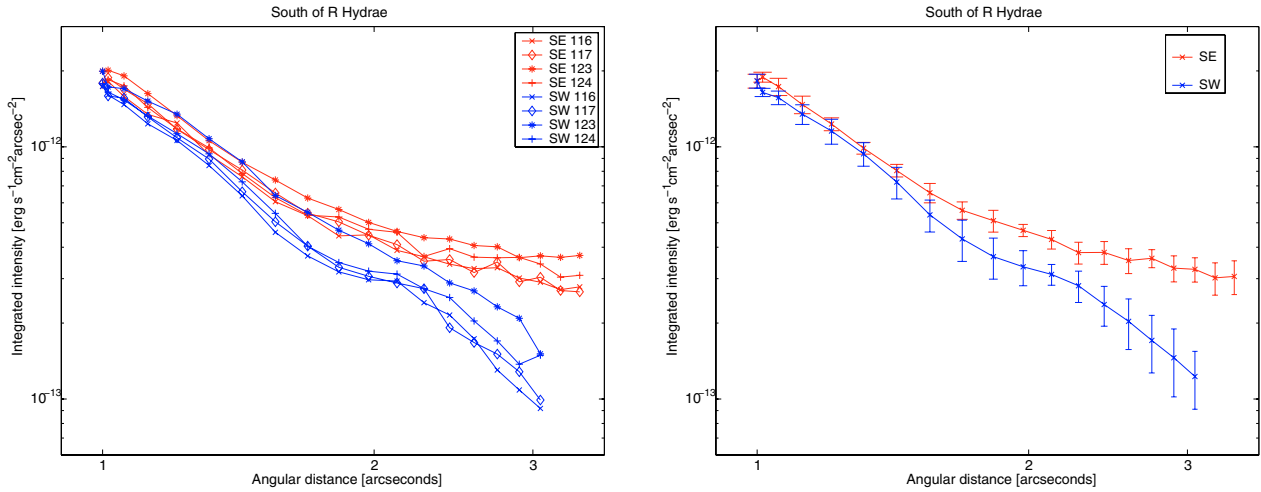


Fig. A.5. Decline of the intensity of the circumstellar emission as a function of angular distance β in the four slits positioned $1''$ to the south of R Hya. *Left:* the decline of the intensity of the four data sets 116, 117, 123, and 124. *Right:* mean (and standard deviation) of the intensity decline of the four south-east (SE) and south-west (SW) scans.

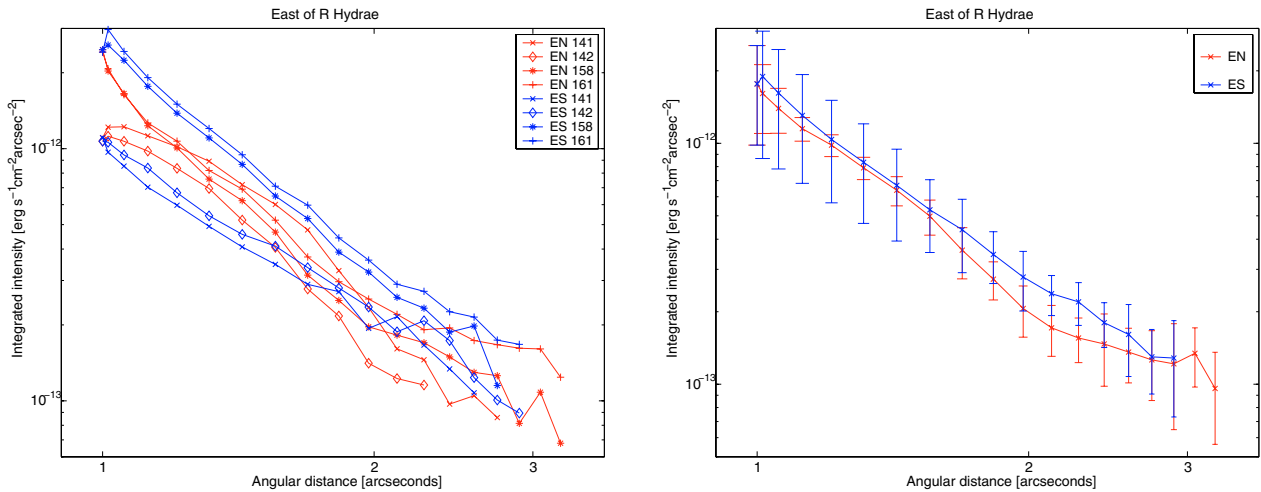


Fig. A.6. Decline of the intensity of the circumstellar emission as a function of angular distance β in the four slits positioned $1''$ to the east of R Hya. *Left:* the decline of the intensity of the four data sets 141, 142, 158, and 161. *Right:* mean (and standard deviation) of the intensity decline of the four east-north (EN) and east-south (ES) scans.

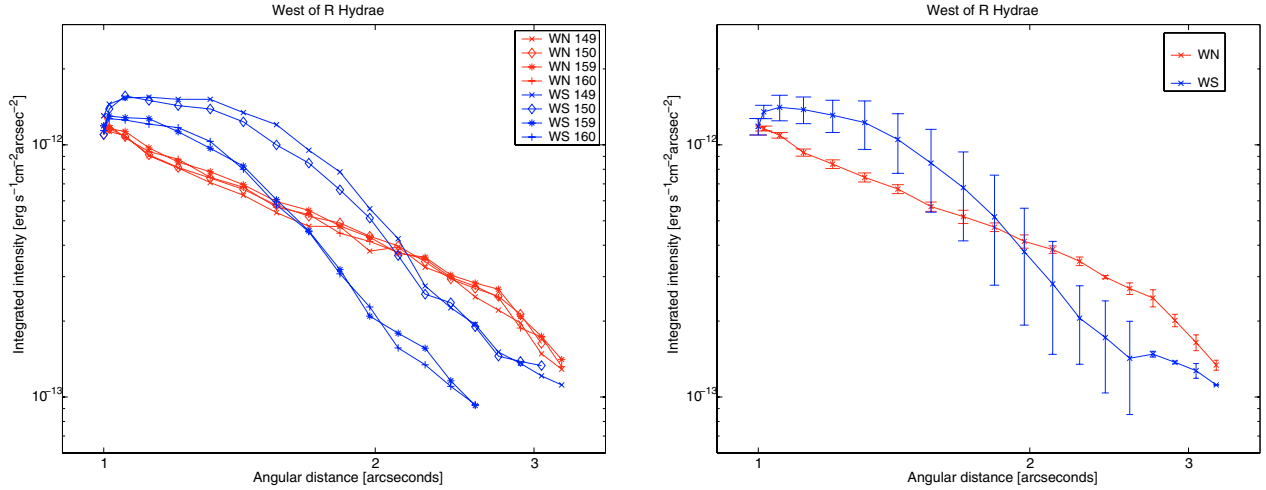


Fig. A.7. Decline of the intensity of the circumstellar emission as a function of angular distance β in the four slits positioned $1''$ to the west of R Hya. *Left:* the decline of the intensity of the four data sets 149, 150, 159, and 160. *Right:* mean (and standard deviation) of the intensity decline of the four west-north (WN) and west-south (WS) scans.

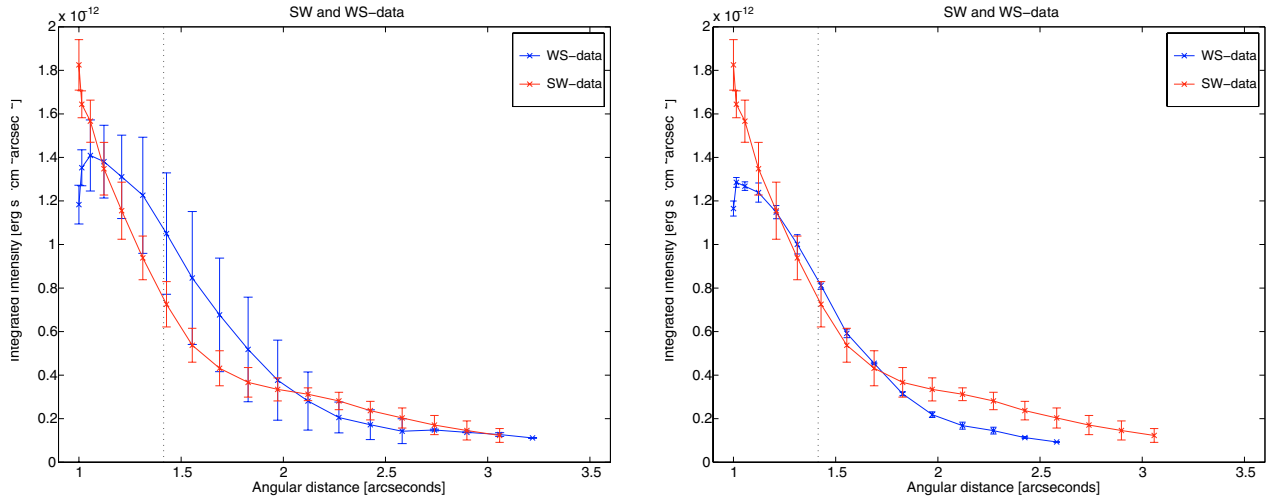


Fig. A.8. Decline of the intensity of the circumstellar CO emission in the south-west and west-south directions of R Hya. *Left:* mean of the (116, 117, 123, 124) and (149, 150, 159, 160) data sets is displayed. At the cross-over points around $1.4''$ from the star, the west-south data are significantly higher than for the south-west scan, due to the higher intensity values of the (149, 150) data sets. *Right:* data sets (149, 150) are omitted. At the cross-over point, the south-west and west-south scans coincides nicely.

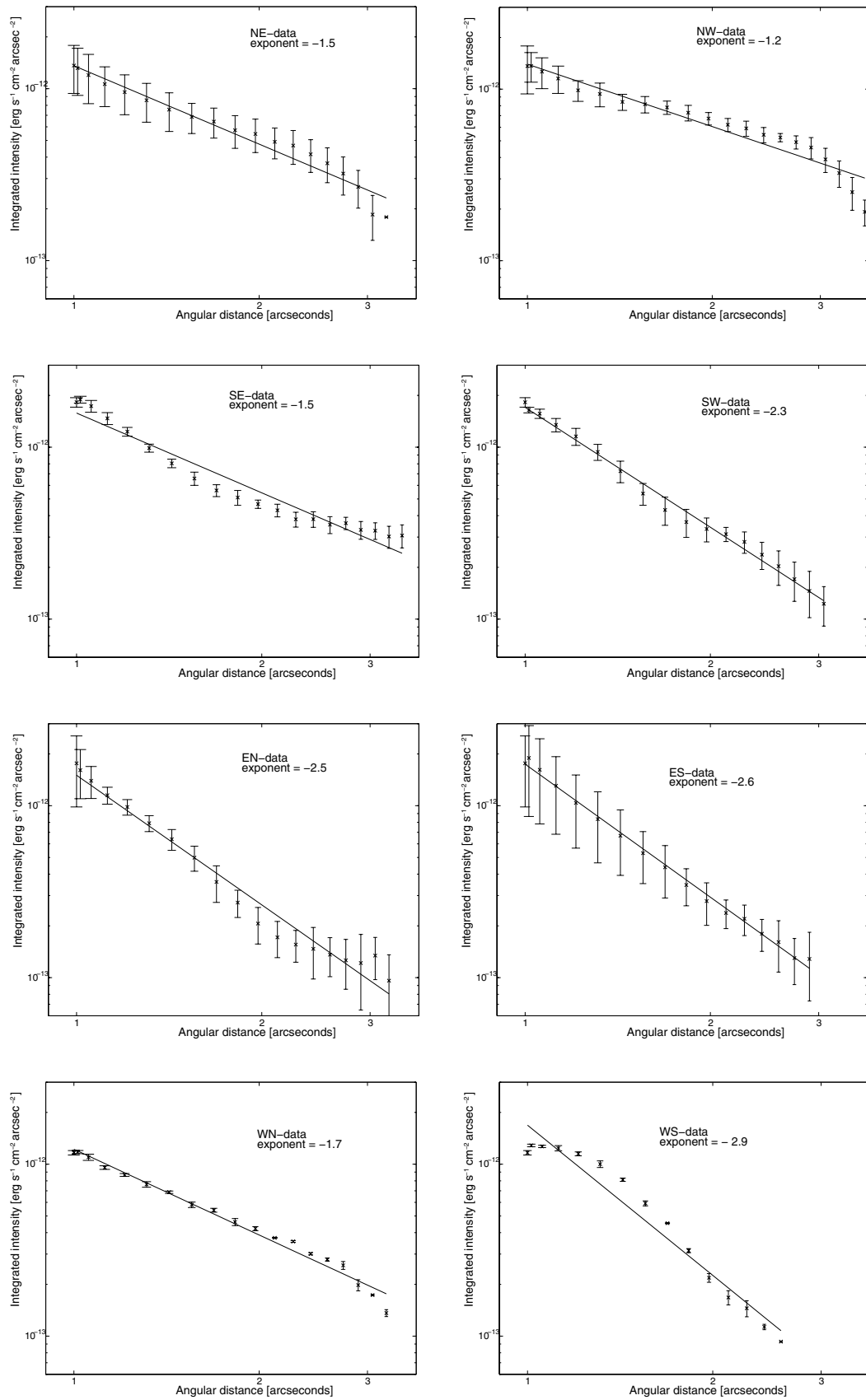


Fig. A.9. Dependence of the scattered wavelength-integrated intensity of the circumstellar CO vibration-rotation lines as a function of the angular distance on the sky, β , for the different scan directions. The straight line represents a β^a power law, with the exponent a specified in each panel.